PRECISION CHEMISTRY

pubs.acs.org/PrecisionChem
Article

Stabilizing Iodine in Pyrochlore: Toward New Nuclear Waste Forms

Published as part of Precision Chemistry special issue "Precision Chemistry for High Entropy Nanomaterials".

Xiao Xu, Guangshuai Han, Tianhao Li, Jiayue Hu, Guotao Qiu, Shao-Yu Tseng, Gyeong Ho Han, Alexander D. Dupuy, Anthony Shoji Hall, and Corey Oses*

Cite This: https://doi.org/10.1021/prechem.5c00467
Read Online

ABSTRACT: The long-term immobilization of iodine-129, a key radionuclide in nuclear waste, remains a major challenge for sustainable nuclear energy. Pyrochlore ceramics, which can be integrated into glass-ceramic waste forms, are widely recognized for their chemical durability and their capacity to immobilize actinides and other long-lived waste elements, but have not previously been demonstrated for iodine. Here, we show iodine can be accommodated into the pyrochlore structure by partial substitution for fluorine in a known oxyfluoride pyrochlore. Structural characterization reveals a solubility limit and associated lattice distortion upon iodine incorporation. To address these constraints, we introduce a high-entropy design strategy and computationally screen over 40,000 multication pyrochlore compositions, identifying candidates with the potential for substantially increased iodine loading. Many candidates exceed 33 wt % iodine, outperforming most existing ceramics, and in principle, iodine loadings as high as 74 wt % are accessible. These results highlight high-entropy pyrochlores as a promising and tunable materials platform for advancing safe and effective immobilization of iodine radionuclides in nuclear waste management.

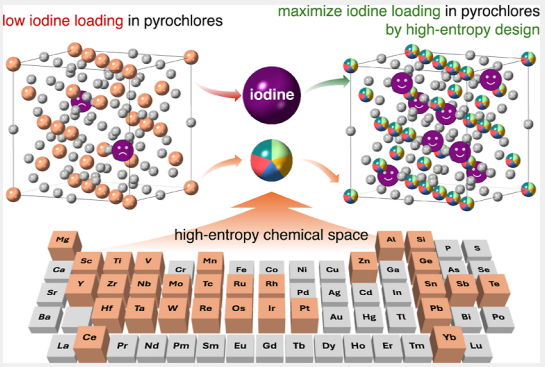

KEYWORDS: *iodine, pyrochlore, nuclear waste immobilization, high-entropy design, lattice distortions*

INTRODUCTION

While nuclear power is regaining attention as a stable low-carbon energy option, significant challenges remain in managing high-level nuclear waste such as spent fuel and reprocessed residues.[1,2] Iodine-129 is a major radionuclide of concern due to its long half-life (15.7 million years),[3] significant fission yield (1% for uranium-235),[4,5] high mobility in water,[6] and strong tendency to accumulate in the human thyroid,[7] making it a persistent health risk over geologic time scales. Unlike uranium and plutonium,[8] iodine-129 is not recycled but is instead captured and immobilized during reprocessing, due to its low economic value and high abundance.[9] Both pure ceramic and pure glass waste forms for iodine-129 suffer limitations, including processing incompatibility, compositional selectivity, insufficient long-term durability, and poor mechanical robustness.[10] Glass-ceramic waste forms, in which one or more durable crystalline phases are embedded within a glassy matrix, offer a promising solution—enabling immobilization of multiple radionuclides and actinides in a robust composite.[11,12]

Pyrochlore is known for its chemical durability, radiation resistance, and compatibility with glass matrices, making it a top choice for glass-ceramic nuclear waste forms.[13−17] Its structural flexibility has enabled the synthesis of many halide-containing forms, including fluoride pyrochlores.[18,19] Unlike perovskite and apatite-type ceramics, which can incorporate iodine,[20−22] pyrochlore has not previously hosted iodine. This has been attributed to the large ionic radius and possible chemical incompatibility of iodide. Addressing these barriers is essential for developing iodine-hosting pyrochlores for nuclear waste forms.

In this work, we report the first synthesis of iodine-containing pyrochlore via hydrothermal methods and directly observe a solubility limit for iodine incorporation in this structure. We find that iodine incorporation leads to lattice distortions and internal stress. To address these limits and explore routes to higher iodine loading, we propose a high-entropy design strategy that leverages multiple-cation disorder to potentially stabilize structures with higher iodide content. By computationally screening over 40,000 high-entropy pyrochlore compositions derived from the full range of reported *B*-site chemistries, we identify a materials design

Received: December 31, 2025
Revised: April 26, 2026
Accepted: May 9, 2026

strategy that, in principle, can significantly boost iodine loading, reduce materials cost, and lessen supply dependence. If validated, this approach could be extended to other material systems, providing a general route for designing robust hosts for challenging waste species.

RESULTS AND DISCUSSION

The pyrochlore structure is often described by the general formula $A_2B_2X_6X'$,[23] where the *A*-site (16*d*) is occupied by eight-coordinated metal ions and the *B*-site (16*c*) by six-coordinated metal ions.[24−26] The more familiar $A_2B_2O_7$ formula[27−29] is a special case in which O^{2-} occupies both the *X* (48*f*) and *X*′ (8*b*) anion sites. However, the pyrochlore framework accommodates a variety of anions at these sites, including F^-, N^{3-}, and S^{2-}, enabling broad chemical flexibility.[18,19,30,31] The structure's corner-sharing BX_6 octahedra create large channels that can host *A*-site cations and *X*′ species.[32,33] This flexibility has enabled the synthesis of halide pyrochlores, such as $Na_2Nb_2O_5F_2$ and $NaCaSb_2O_6F$.[18,19] However, the much larger ionic radius of iodide (2.2 Å) compared to fluoride (1.3 Å) is expected to present a significant challenge for incorporation.

Motivated by this structural flexibility and prior halide substitutions,[26] we hypothesized that iodide could, at least partially, be incorporated into the pyrochlore lattice despite its larger radius. To test the limits of iodide uptake, we synthesized seven samples with varying iodide-to-fluoride ratios using hydrothermal methods (Table 1). For brevity,

Table 1. Sample Naming Scheme for Iodine-Containing Pyrochlores[a]

nominal stoichiometries	I^- replacement	I^-:F^- ratio	label
$Na_2Nb_2O_5F_2$	0%	0:2	O_5F_2
$Na_2Nb_2O_5F_{1.9}I_{0.1}$	5%	0.1:1.9	$O_5F_{1.9}I_{0.1}$
$Na_2Nb_2O_5F_{1.8}I_{0.2}$	10%	0.2:1.8	$O_5F_{1.8}I_{0.2}$
$Na_2Nb_2O_5F_{1.7}I_{0.3}$	15%	0.3:1.7	$O_5F_{1.7}I_{0.3}$
$Na_2Nb_2O_5FI$	50%	1:1	$O_5F_1I_1$
$Na_2Nb_2O_5F_{0.5}I_{1.5}$	75%	1.5:0.5	$O_5F_{0.5}I_{1.5}$
$Na_2Nb_2O_5I_2$	100%	2:0	O_5I_2

[a]Each label corresponds to a nominal stoichiometry, the percentage of F^- replaced by I^-, and the I^-:F^- ratio in the precursor solution. Na and Nb are omitted from the labels for clarity.

we refer to each composition by a label defined in Table 1 (e.g., $O_5F_{1.8}I_{0.2}$ corresponds to $Na_2Nb_2O_5F_{1.8}I_{0.2}$). The hydrothermal method uses low temperatures[34] and a sealed environment,[35] which minimizes iodine volatilization[36] and aids iodide incorporation.

We characterized phase by X-ray diffraction (XRD), morphology by scanning electron microscopy (SEM), local lattice distortions by Raman spectroscopy, and iodide incorporation and chemical states by X-ray photoelectron spectroscopy (XPS). We used XPS rather than energy-dispersive X-ray spectroscopy (EDS) because EDS has low sensitivity and overlapping peaks for iodine, while XPS can unambiguously identify and quantify iodine in the samples.

Phase Formation

XRD was used to determine phase formation and identify structural changes resulting from iodide incorporation. XRD patterns for all samples and the Nb_2O_5 precursor are shown in Figure 1a. O_5F_2 matches the reported pattern for pyrochlore $Na_2Nb_2O_5F_2$,[18] confirming formation of the $Fd\bar{3}m$ pyrochlore phase. Samples with up to 15% iodide ($O_5F_{1.9}I_{0.1}$, $O_5F_{1.8}I_{0.2}$, $O_5F_{1.7}I_{0.3}$) also closely match the reference pyrochlore pattern. O_5I_2 matches the pristine Nb_2O_5 precursor (orthorhombic *Pbam*),[37] indicating little or no reaction. The intermediate samples with 50% or more iodide ($O_5F_1I_1$ and $O_5F_{0.5}I_{1.5}$) show a mixture of the two reference profiles ($Fd\bar{3}m$ and *Pbam*), indicating partial reaction.

For O_5F_2, $O_5F_{1.9}I_{0.1}$, $O_5F_{1.8}I_{0.2}$, and $O_5F_{1.7}I_{0.3}$, peak shifts and Rietveld-refined lattice parameters (Figure 1b,c) indicate an initial lattice expansion with increasing iodide content,[38] followed by contraction at higher iodide levels.[39] We interpret these results as follows: at low iodide content, iodide replaces fluoride, and the larger ionic radius of iodide causes lattice expansion. When the solubility limit is reached (near $O_5F_{1.8}I_{0.2}$), additional iodide can no longer be accommodated in the pyrochlore lattice. Instead, further increase in nominal iodide content is associated with vacancy formation, leading to lattice contraction and destabilization of the pyrochlore phase. This mechanistic interpretation is summarized in the schematic model shown in Figure 1d. As supported by the XPS analysis and related discussion presented in the following sections, iodide can be incorporated into the pyrochlore lattice up to a solubility limit; above this limit, vacancy formation becomes favorable and the pyrochlore phase becomes less stable.

Morphology

SEM was performed to evaluate particle morphology and assess the preservation of pyrochlore microstructure. SEM images for all samples and the Nb_2O_5 precursor are shown in Figure 2. O_5F_2 shows uniform octahedral particles, consistent with reference $Na_2Nb_2O_5F_2$[18,40] (Figure 2a). Similarly, $O_5F_{1.9}I_{0.1}$, $O_5F_{1.8}I_{0.2}$, and $O_5F_{1.7}I_{0.3}$ (Figure 2b−d) display pyrochlore-like morphology. However, samples with higher iodide content ($O_5F_1I_1$, $O_5F_{0.5}I_{1.5}$, O_5I_2; Figure 2e−g) show increased morphological heterogeneity and irregular, nonuniform particles. O_5I_2 shows no pyrochlore-like features, and the morphology resembles unreacted Nb_2O_5 precursor (Figure 2h). These observations are consistent with XRD results: pyrochlore morphology is maintained at low iodide content, but is disrupted at higher iodide fractions.

Local Lattice Distortions

To investigate whether iodide incorporation causes lattice distortion in the structure, we performed Raman spectroscopy (Figure 3a). We focus on the broad, asymmetric band near 680 cm^{-1}, which is assigned to Nb−O−Nb stretching vibrations[41] and reflects the corner-sharing BX_6 octahedra framework in pyrochlore (Figure 3b). The observed spectra confirm that O_5F_2, $O_5F_{1.9}I_{0.1}$, $O_5F_{1.8}I_{0.2}$, and $O_5F_{1.7}I_{0.3}$ all adopt the pyrochlore structure.[42] We analyze the full width at half-maximum (FWHM) of this peak, as peak broadening is an indicator of increased local distortion.[43−47] As shown in Figure 3c, the FWHM increases from O_5F_2 to $O_5F_{1.8}I_{0.2}$, indicating that iodide incorporation enhances local lattice distortion. At $O_5F_{1.7}I_{0.3}$, the FWHM decreases, consistent with reduced incorporation of iodide and a slower increase in lattice distortion. This trend in FWHM supports the iodide-incorporation model proposed from XRD (Figure 1d): iodide substitution induces local distortion in the pyrochlore lattice up to the solubility limit, beyond which additional iodide is not incorporated and lattice distortion is alleviated.

https://doi.org/10.1021/prechem.5c00467
Precis. Chem. XXXX, XXX, XXX−XXX

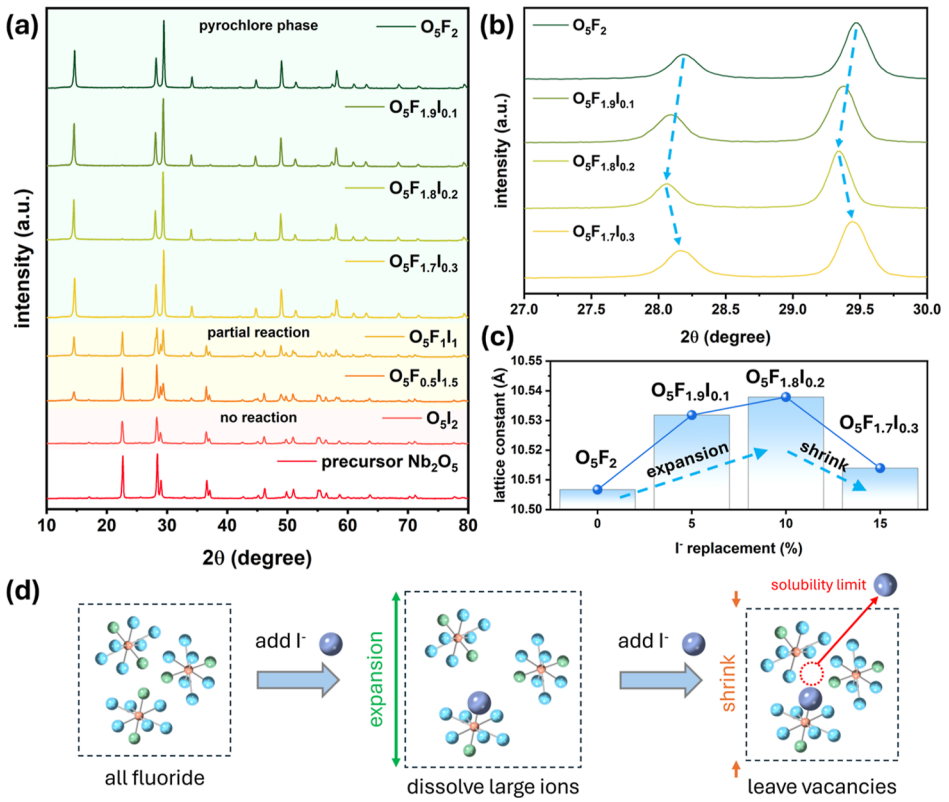

Figure 1. X-ray diffraction (XRD) results for iodine-containing oxyfluoride pyrochlores. (**a**) XRD patterns for all samples with varying iodine-to-fluoride ratios. Na and Nb are omitted from sample annotations for clarity; only the *X*- and *X*′-site anions are shown (e.g., $O_5F_{1.9}I_{0.1}$ denotes $Na_2Nb_2O_5F_{1.9}I_{0.1}$). (**b**) Enlarged XRD profiles for samples with a single pyrochlore phase; peak shifts are highlighted with blue arrows. (**c**) Lattice parameters extracted by Rietveld refinement of the XRD patterns. (**d**) Schematic illustration of the lattice parameter evolution mechanism during iodide incorporation in the pyrochlore structure. Dark blue, light blue, green, and orange spheres represent iodide, oxide, fluoride, and sodium ions, respectively. To highlight the changes at both the *X* and *X*′ sites, only the $AX_6X'_2$ dodecahedron unit is depicted.

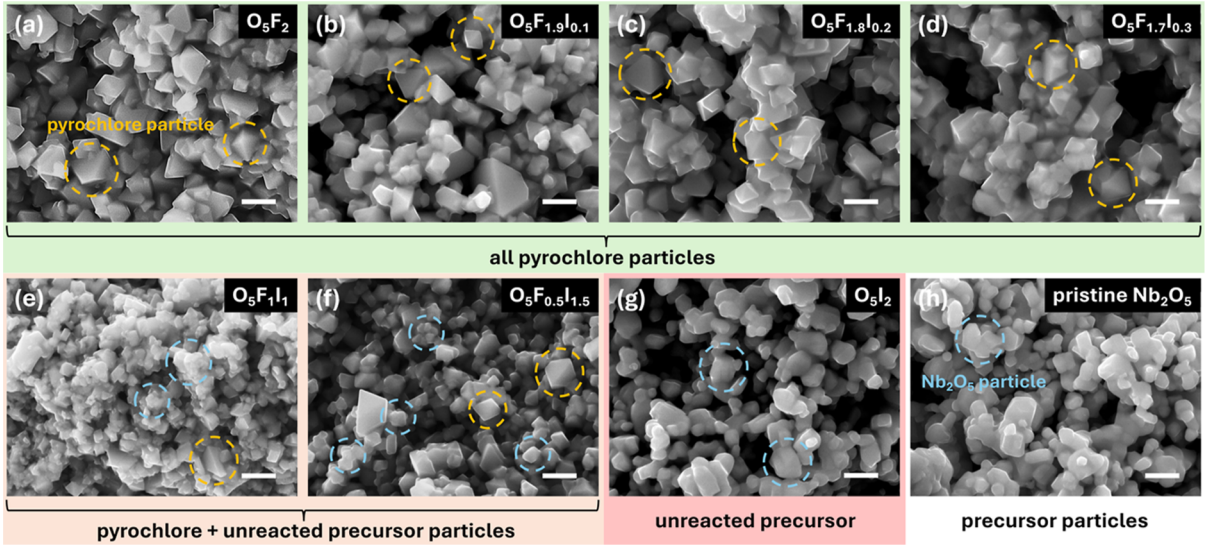

Figure 2. Scanning electron microscopy (SEM) images of iodine-containing pyrochlores. SEM images of (**a**) O_5F_2, (**b**) $O_5F_{1.9}I_{0.1}$, (**c**) $O_5F_{1.8}I_{0.2}$, (**d**) $O_5F_{1.7}I_{0.3}$, (**e**) $O_5F_1I_1$, (**f**) $O_5F_{0.5}I_{1.5}$, (**g**) O_5I_2, and (**h**) pristine Nb_2O_5. All scale bars are 500 nm.

Iodide Incorporation

XPS was used to identify the presence of elements, assess oxidation states, and investigate the local chemical environment.[48,49] XPS measurements for $O_5F_{1.9}I_{0.1}$, $O_5F_{1.8}I_{0.2}$, and $O_5F_{1.7}I_{0.3}$ show clear iodine 3d signals (Figure 3d), confirming the incorporation of iodide. Compositional uniformity was assessed by EDS mapping of $O_5F_{1.7}I_{0.3}$, as shown in Figure S3. For the eight-coordinated Na site, negative binding energy shifts are observed in $O_5F_{1.8}I_{0.2}$ and $O_5F_{1.7}I_{0.3}$ (Figure 3e), which are characteristic of a decrease in the effective positive charge[50] and suggest a modification of the local electronic environment near the iodide solubility limit. To probe this, we

https://doi.org/10.1021/prechem.5c00467
Precis. Chem. XXXX, XXX, XXX−XXX

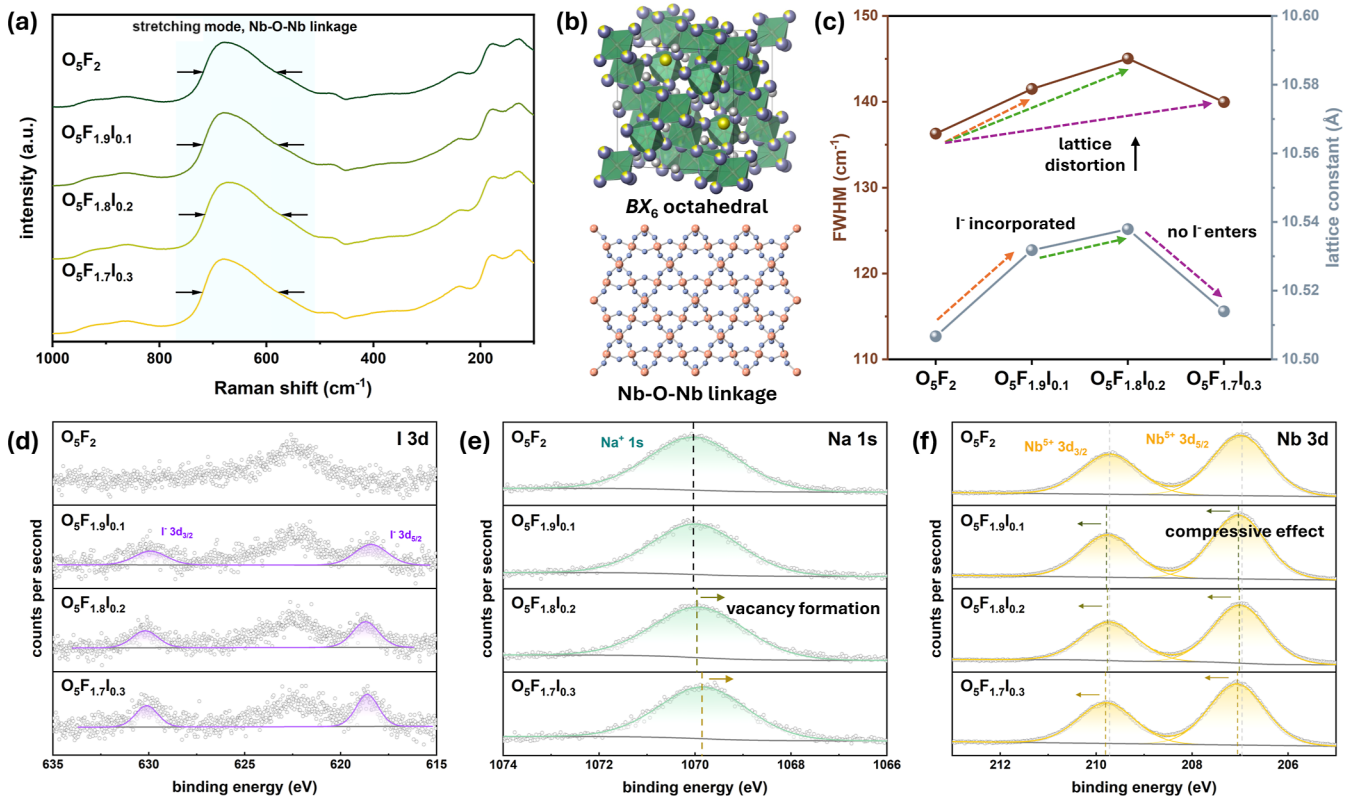

Figure 3. Raman spectra and X-ray photoelectron spectroscopy (XPS) results. (**a**) Full Raman spectra of O_5F_2, $O_5F_{1.9}I_{0.1}$, $O_5F_{1.8}I_{0.2}$, and $O_5F_{1.7}I_{0.3}$. (**b**) Schematic of the pyrochlore structure, highlighting the BX_6 octahedra and Nb−O−Nb linkages. (**c**) Evolution of the Raman full width at half-maximum (FWHM) with lattice constant, extracted from XRD. (**d**-**f**) High-resolution XPS spectra for (**d**) I 3d, (**e**) Na 1s, and (**f**) Nb 3d orbitals for O_5F_2, $O_5F_{1.9}I_{0.1}$, $O_5F_{1.8}I_{0.2}$, and $O_5F_{1.7}I_{0.3}$.

performed a detailed analysis of the O 1s spectrum, as shown in Figure S4. In pyrochlore, the O 1s signal can be resolved into two components: a lower-binding-energy component attributed to lattice oxygen (O_{latt}) and a higher-binding-energy component attributed to adsorbed oxygen species (O_{ads}).[51,52] The latter is often attributed to surface adsorbates and can be influenced by defect chemistry.[51,52] We quantified the relative peak area ratios of O_{ads} to O_{latt} to evaluate the adsorbed oxygen content in each sample, and the results are summarized in Table S1. $O_5F_{1.7}I_{0.3}$ exhibits the highest O_{ads}/O_{latt} ratio (0.86), exceeding those of $O_5F_{1.8}I_{0.2}$ (0.76), $O_5F_{1.9}I_{0.1}$ (0.72), and O_5F_2 (0.72). These results indicate a higher concentration of adsorbed oxygen is present in $O_5F_{1.7}I_{0.3}$, reflecting increased surface adsorbates and changes in the local chemical environment, potentially influenced by defect chemistry. If vacancy formation occurs, prior studies suggest that vacancies would preferentially form at the X' site, as vacancy formation at the X' site is more favorable for maintaining the structural stability of the pyrochlore.[53] This interpretation is consistent with prior descriptions of anion-site occupancy in pyrochlores[54,55] and is further supported by a study on oxyfluoride pyrochlores showing that, upon the introduction of anion vacancies, they occupy the X' site rather than the X site.[56] For Nb^{5+}, positive binding energy shifts in $O_5F_{1.9}I_{0.1}$, $O_5F_{1.8}I_{0.2}$, and $O_5F_{1.7}I_{0.3}$ are observed (Figure 3f), which are attributed to compressive strain induced by the larger iodide ions.[57] These results are consistent with the proposed mechanism in Figure 1d, in which vacancy formation may occur once the solubility limit is reached, leading to lattice contraction upon further iodine incorporation.

Chemical Stability

To evaluate the chemical stability of our synthesized materials, we selected $O_5F_{1.7}I_{0.3}$ and measured its iodine leaching rate, as shown in Figure S5. The measured leaching rate at 150 °C after 3 days was 1.07×10^{-4} g m^{-2} d^{-1}. This value is lower than those reported for several ceramic waste forms in the literature.[10] For example, it is lower than those reported for iodosodalite $Na_4(AlSiO_4)_3I$ (7.9×10^{-4} g m^{-2} d^{-1}),[58] perovskite $Cs_3Bi_2I_9$ (hydroxyapatite composite, ~0.6 g m^{-2} d^{-1}),[59] iodoapatite $Pb_{10}(VO_4)_6I_2$ (0.398 g m^{-2} d^{-1}),[22] glass-bonded sodalite (0.8 g m^{-2} d^{-1}),[60] and iodosodalite with bismuthate glass (8.8×10^{-4} g m^{-2} d^{-1}).[61] These results indicate good chemical durability of the iodine-containing pyrochlore under the present test conditions. They also suggest that structurally incorporated iodine remains relatively stable under the present test conditions.

OUTLOOK

Radiation Resistance

Materials for nuclear waste immobilization must exhibit good resistance to radiation, as irradiation can gradually alter composition and degrade structural integrity over time. Ceramic materials generally possess robust crystal structures that are relatively resistant to radiation-induced deformation.[77,78] In particular, a niobium-containing oxide with a fluorite-derived structure has been demonstrated to exhibit high radiation resistance.[79] Pyrochlore is closely related to the fluorite structure and has also been reported to exhibit excellent radiation resistance under extreme conditions.[78,80−82]

https://doi.org/10.1021/prechem.5c00467
Precis. Chem. XXXX, XXX, XXX−XXX

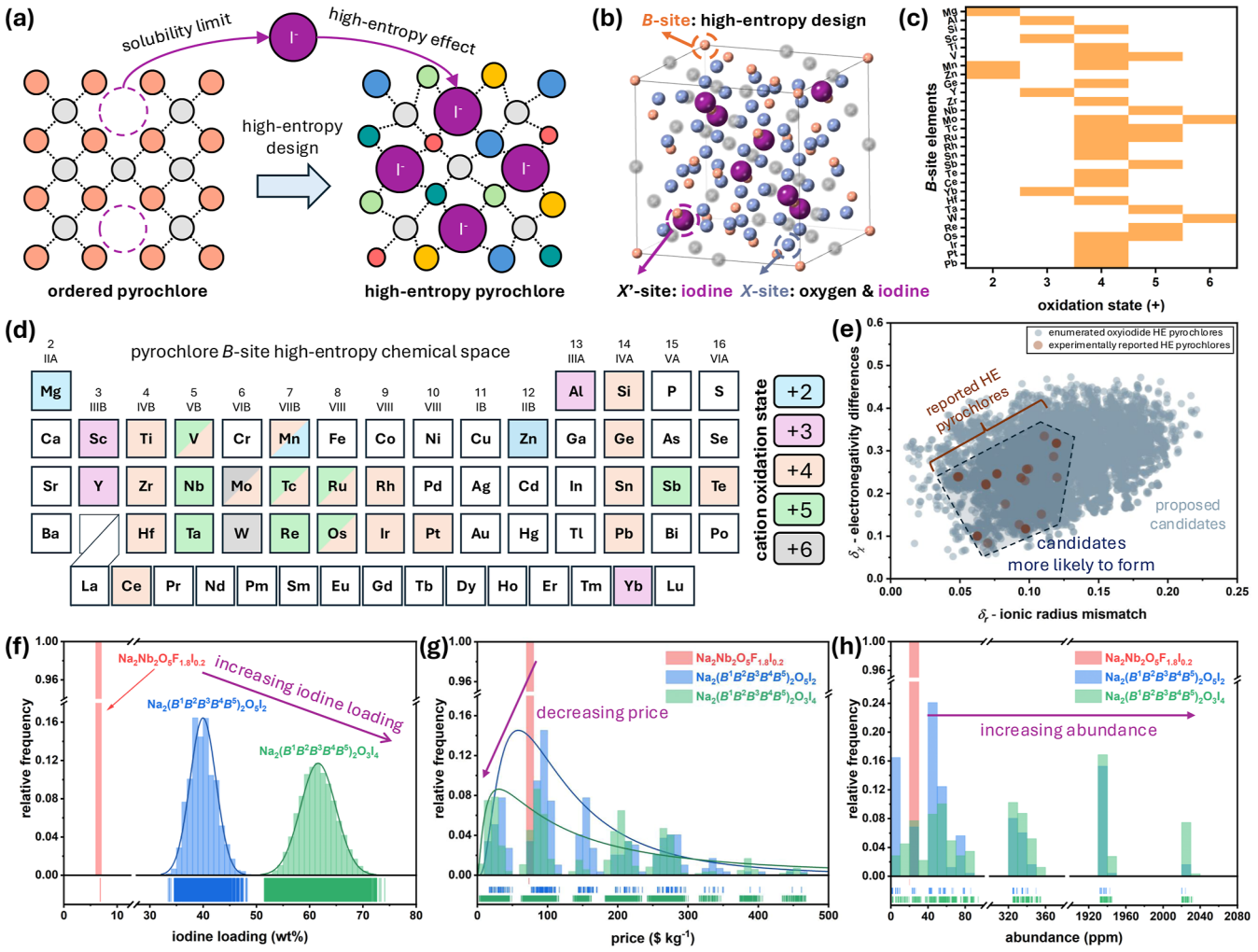

Figure 4. Future outlook for high-entropy design to enhance iodine loading. (**a**) Schematic showing enhanced iodine incorporation in a lattice through high-entropy design. (**b**) Crystallographic sites available to iodine in the pyrochlore structure; high-entropy design is illustrated for the *B*-site at the center of the BX_6 octahedra framework. (**c**) All *B*-site elements and their oxidation states observed in reported high-entropy pyrochlores, highlighting compositional diversity. (**d**) Periodic table map of *B*-site elements with color coding for accessible oxidation states; these represent all potential candidates for high-entropy design. (**e**) Descriptor-space plot of enumerated iodine-containing high-entropy pyrochlore compositions and known high-entropy pyrochlores,[62−76] using weighted-average ionic radius and electronegativity difference. The dashed blue region marks an area for future exploration where known and candidate compositions overlap. (**f**) Iodine-loading distribution for candidate pyrochlores, showing the potential boost from high-entropy design. (**g**) Average price among high-entropy candidate compositions. (**h**) Average elemental abundance in Earth's crust for the candidates.

On this basis, the Nb-based iodine-containing pyrochlore synthesized in the present work may also be expected to exhibit good radiation resistance, although direct experimental validation will be needed. Glass-ceramic waste forms based on iodine-containing pyrochlores may also be promising for the long-term containment of hazardous radionuclides. Incorporating niobium-containing compounds into glass systems has been reported to enhance overall radiation resistance.[83]

High-Entropy Design

Our results reveal the mechanisms underlying the low iodide loading in pyrochlores and clarify the central challenge for developing higher capacity nuclear waste forms. The large size of iodide relative to fluoride imposes a strict solubility limit in the pyrochlore structure. Only a small fraction of fluoride sites can be replaced by iodide before the lattice strain becomes unsustainable. Beyond this point, additional iodide induces vacancy formation and, ultimately, prevents further integration of iodide or formation of the pyrochlore phase. This progression from lattice distortion to vacancy formation to the appearance of unreacted precursor at high iodide concentrations explains the observed limit to iodide immobilization in these materials.

Overcoming this challenge and enabling stable, high-iodide nuclear waste forms requires a strategy that can accommodate substantial lattice distortions and energetic barriers. High-entropy materials (Figure 4a) provide such a pathway by the random mixing of multiple elements on the same crystallographic site in (near-)equimolar ratios, leading to high configurational entropy.[34,84] This entropy allows stabilization of structures with large enthalpic penalties and severe lattice distortion. Large lattice distortion is one of the four core effects in high-entropy materials and is associated with beneficial properties such as increased hardness and low lattice thermal conductivity.[85,86]

Studies in high-entropy ceramics show that the anion sublattice (e.g., oxygen[87] or carbon[88]) acts as a structural buffer

https://doi.org/10.1021/prechem.5c00467
Precis. Chem. XXXX, XXX, XXX−XXX

between cations. It develops significant local distortions to accommodate multiple, chemically diverse cations, while the cation sublattice remains nearly ideally distributed. This buffering enables the introduction of additional cation species.[89] Our aim is to explore the converse: the introduction of additional cation species may enable the stabilization of phases with substantial lattice distortions localized in the anion sublattice, thereby facilitating higher levels of iodide incorporation.

High-entropy materials have also been shown to offer other critical properties for nuclear waste immobilization. For example, $(Sm_{0.19}Gd_{0.19}Dy_{0.19}Er_{0.19}Yb_{0.19}U_{0.05})_2Ti_2O_7$[90] and $(Sm,Yb,Gd,Er,Dy)_2Zr_2O_7$[91] show improved leaching resistance and chemical durability. $Gd_2(Ti_{0.25}Zr_{0.25}Hf_{0.25}Ce_{0.25})_2O_7$[69] and $(Lu_{0.2}Yb_{0.2}Er_{0.2}Y_{0.2}Gd_{0.2})PO_4$[92] demonstrate high corrosion resistance, while $(Nd_{0.25}Sm_{0.25}Eu_{0.25}Gd_{0.25})_2Zr_2O_7$[93] and $(Lu_{0.2}Yb_{0.2}Er_{0.2}Y_{0.2}Gd_{0.2})PO_4$ also exhibit high radiation stability.

The pyrochlore structure comprises two cation sublattices—the *A* site (typically large rare earth or alkaline earth cations) and the *B* site (generally smaller transition metal cations). Both cation sites can accommodate multiple species in a high-entropy configuration:[62,68] for example, $(Sm_{0.2}Eu_{0.2}Gd_{0.2}Y_{0.2}Lu_{0.2})_2Ti_2O_7$[68] demonstrates *A*-site mixing and $La_2(Hf_{0.2}Nb_{0.2}Sc_{0.2}Sn_{0.2}Zr_{0.2})_2O_7$[62] demonstrates *B*-site mixing. Here, we focus on the *B* site (Figure 4b) because it offers a broad range of transition metal chemistries and lighter cations, maximizing both compositional diversity and the achievable iodine loading by weight. The *B*-site cations also form the BX_6 octahedral network, which is central to the pyrochlore's structural flexibility and governs the ability to accommodate large anions such as iodide.

We surveyed the literature for *B*-site cations present in reported halide-containing and high-entropy pyrochlores, identifying 29 elements spanning accessible oxidation states from 2+ to 6+ (Table 2). Although no iodine-containing pyrochlore has been reported, several fluoride analogues exist, such as $A_2B_2O_6F$,[94] $A_2B_2O_5F_2$,[18] and $AB_2O_3F_3$.[95] Figure 4c displays each *B*-site element and its observed oxidation states in these materials, providing a vast compositional space for new high-entropy candidates (Figure 4d). Most reported high-entropy pyrochlores differ from the Na-based oxyhalide platform studied here in their cation-valence chemistry, often featuring trivalent *A*-site cations and tetravalent *B*-site cations. By contrast, the accessible design space for halide-containing high-entropy pyrochlores has not yet been established.

For the candidate library, we focused on five-metal equimolar mixtures of *B*-site cations for $Na_2\{B\}_2O_5I_2$ and $Na_2\{B\}_2O_3I_4$ anion site configurations. Sodium was chosen for the *A* site for several reasons: (1) Na occupies the *A* site of our benchmark halide-containing pyrochlore $Na_2Nb_2O_5F_2$ and thus can serve as an anchor between computational design and experimental validation; (2) Na is one of the lightest *A*-site elements reported inoxyhalide pyrochlores, maximizing possible iodine loading by weight; (3) compared with lighter Li, Na is more abundant and significantly less expensive; and (4) Na is a frequent glass modifier, lowering melting temperatures and improving processability and workability, promoting glass-ceramic formation for nuclear waste immobilization. The following criteria were applied to achieve charge neutrality: (i) $Na_2(B^1B^2B^3B^4B^5)_2O_5I_2$ must have *B*-site cations summing to 10+ per formula unit (e.g., five 5+ cations; or two 4+, two 5+, one 6+); (ii) $Na_2(B^1B^2B^3B^4B^5)_2O_3I_4$ must have *B*-site cations totaling 8+ per formula unit (e.g., five 4+ cations; or one each of 2+, 3+, 4+, 5+, 6+). We focus on the O_5I_2 anion configuration because it preserves the same structural motif as our benchmark halide-containing pyrochlore $Na_2Nb_2O_5F_2$. To further increase iodine content, we also consider the hypothetical O_3I_4 configuration, which pushes the boundary of possible iodine incorporation within the high-entropy design space. We did not include the O_4I_3 anion configuration

Table 2. Summary of *B*-Site Elements and Their Observed Oxidation States in Reported Oxide, Oxyfluoride, and High-Entropy Oxide Pyrochlores[a]

compound	*B*-site parent element	oxidation state	classification
$La_2(ZnMgHfWMo)_2O_7$[76]	Mg	+2	high-entropy oxide
$(Y, Er)_2(TiGeSnAlNb)_2O_7$[67]	Al	+3	high-entropy oxide
$(Sc, In)_2Si_2O_7$[98]	Si	+4	oxide
$La_2(HfNbScSnZr)_2O_7$[62]	Sc	+3	high-entropy oxide
$La_2Ti_2O_7$,[99] $Yb_2Ti_2O_7$,[100] $Bi_2Ti_2O_7$[101]	Ti	+4	oxide
$(Y, Er, Dy)_2V_2O_7$,[102] $Zn_2V_2O_7$[103]	V	+4, +5	oxide
$(Y, In, Lu, Tl)_2Mn_2O_7$,[104,105] $Sc_2Mn_2O_7$,[106] $CsMnMoO_3F_3$[95]	Mn	+2, +4	oxide, oxyfluoride
$CsZnMoO_3F_3$,[95] $La_2(ZnMgHfWMo)_2O_7$[76]	Zn	+2	oxyfluoride, high-entropy oxide
$In_2Ge_2O_7$[107]	Ge	+4	oxide
$La_2(YbYZrNbTa)_2O_7$[64]	Y	+3	high-entropy oxide
$Ce_2Zr_2O_7$,[108] $La_2Zr_2O_7$,[99] $Nd_2Zr_2O_7$,[109] $Pr_2Zr_2O_7$[110]	Zr	+4	oxide
$Sn_2Nb_2O_7$,[111] $Cd_2Nb_2O_7$,[112] $Na_2Nb_2O_5F_2$[18]	Nb	+5	oxide, oxyfluoride
$(Dy, Gd, Sm, Nd)_2Mo_2O_7$,[113] $CsZnMoO_3F_3$,[95] $CsMnMoO_3F_3$,[95] $La_2(ZnMgHfWMo)_2O_7$[76]	Mo	+4, +6	oxide, oxyfluoride
$Sm_2Tc_2O_7$,[114] $Cd_2Tc_2O_7$[115]	Tc	+4, +5	oxide
$Bi_2Ru_2O_7$,[116] $Ca_2Ru_2O_7$,[117] $Hg_2Ru_2O_7$,[118] $Sm_2Ru_2O_7$,[119] $(Pr, Nd, Eu, Gd, Tb, Ho)_2Ru_2O_7$[120,121]	Ru	+4, +5	oxide
$Bi_2Rh_2O_{6.8}$[122]	Rh	+4	oxide
$(La, Pr, Sm, Y)_2Sn_2O_7$[123,124]	Sn	+4	oxide
$Cd_2Sb_2O_7$,[125] $(Co, Mn, Ni)_2Sb_2O_7$,[126] $Hg_2Sb_2O_7$[127]	Sb	+5	oxide
$Pr_2Te_2O_7$[128]	Te	+4	oxide
$Nd_2(TiZrHfCe)_2O_7$[68]	Ce	+4	high-entropy oxide
$La_2(YbYZrNbTa)_2O_7$[64]	Yb	+3	high-entropy oxide
$(Sm, Eu, Gd)_2Hf_2O_7$[129]	Hf	+4	oxide
$Ca_2Ta_2O_7$,[130] $Cd_2Ta_2O_7$,[112] $Sn_2Ta_2O_7$,[111] $Na_2Ta_2O_5F_2$[18]	Ta	+5	oxide, oxyfluoride
$La_2(ZnMgHfWMo)_2O_7$[76]	W	+6	high-entropy oxide
$Cd_2Re_2O_7$,[131,132] $Pb_2Re_2O_{7-x}$[133]	Re	+5	oxide
$Hg_2Os_2O_7$,[134] KOs_2O_6,[135] $Tl_2Os_2O_7$[136]	Os	+4, +5	oxide
$Er_2Ir_2O_7$,[137] $(Pr, Nd, Eu, Gd, Tb, Ho)_2Ir_2O_7$,[120] $Y_2Ir_2O_7$[138]	Ir	+5	oxide
$Eu_2Pt_2O_7$[139]	Pt	+4	oxide
$Bi_2Pb_2O_7$[140]	Pb	+4	oxide

[a]This table reports the *B* elements, typical oxidation states, and classification for each representative compound.

https://doi.org/10.1021/prechem.5c00467
Precis. Chem. XXXX, XXX, XXX−XXX

Table 3. Top-Ranked High-Entropy Iodine-Containing Pyrochlore Candidates Identified by Combined Performance Metrics[a]

composition	δ_χ	δ_r	cost (USD kg^{-1})	abundance (ppm)	iodine loading (wt %)
$Na_2(AlMnNbSiTi)_2O_3I_4$	0.203	0.114	18.04	106515.8	72.33
$Na_2(AlMgMoNbSi)_2O_3I_4$	0.214	0.109	23.88	107779.6	71.62
$Na_2(AlMnSbSiTi)_2O_3I_4$	0.217	0.093	4.50	106515.8	71.16
$Na_2(AlNbSiTiZr)_2O_3I_4$	0.218	0.137	24.96	106504.7	70.87
$Na_2(AlMgMoSbSi)_2O_3I_4$	0.262	0.094	10.34	107779.6	70.47
$Na_2(MoNbSiTiW)_2O_5I_2$	0.197	0.102	32.40	96624.9	45.40
$Na_2(MnMoNbSiW)_2O_5I_2$	0.196	0.119	30.48	96455.3	45.17
$Na_2(MoSbSiTiW)_2O_5I_2$	0.253	0.088	18.86	96624.9	44.48
$Na_2(MnMoSbSiW)_2O_5I_2$	0.216	0.103	16.94	96455.2	44.26
$Na_2(MoNbSiWZr)_2O_5I_2$	0.207	0.128	37.40	96443.6	44.04

[a]The table lists the five best O_3I_4 and five best O_5I_2 compositions, ranked by predicted iodine loading. For each candidate, the *B*-site elements, electronegativity difference (δ_χ), and ionic radius mismatch (δ_r) are shown; δ_χ and δ_r are Hume−Rothery-type stability descriptors calculated from the *B*-site components. Estimated raw-material cost (USD kg^{-1}) and elemental abundance (ppm) are the weighted means for the *B*-site elements. All data were obtained from the `mendeleev` Python library.[141]

because it requires a total *B*-site charge of +9 (i.e., an average of +4.5 per *B*-site cation), which is difficult to achieve.

The total candidate library includes 41,413 high-entropy compositions: 38,797 with O_3I_4 stoichiometry and 2616 with O_5I_2. The much larger number of O_3I_4 candidates reflects the greater flexibility in charge balancing in this group, which permits a broader combination of *B*-site chemistries. Benchmarking against $O_5F_{1.8}I_{0.2}$, the highest iodine-loaded pyrochlore synthesized in this work (6.85 wt % iodine), we find that theoretical loading for a maximal $Na_2(B^1B^2B^3B^4B^5)_2O_3I_4$ composition can reach as high as 74 wt %. Even a single experimentally viable high-entropy composition would enable iodine loading above 33 wt %, surpassing most existing ceramic materials for iodine immobilization.[22,58,96]

We screened these compositions using Hume−Rothery-type stability descriptors: *B*-site electronegativity difference (δ_χ) and ionic radius mismatch (δ_r) (Figure 4e). This approach helps identify systems more likely to form a single-phase high-entropy pyrochlore over phase separating. Although these simple composition-based descriptors do not reliably predict synthesizability, they are useful for highlighting regions of composition space where single-phase high-entropy pyrochlores have been reported.[97] We defined our region of interest by overlaying reported high-entropy pyrochlores in this descriptor space, and found that this region aligns with low values of δ_χ and δ_r. This supports the Hume−Rothery logic that minimizing *B*-site heterogeneity and enthalpic penalties is key to stabilizing single-phase high-entropy pyrochlores. For all candidates, we then evaluated and compared theoretical iodine loading, cost, and elemental abundance, benchmarking against $O_5F_{1.8}I_{0.2}$, the highest iodine-loaded pyrochlore in this work (6.85 wt % iodine, Figure 4f−h).

After applying all screening criteria, we focused on candidate compositions from the region of interest that also have estimated cost and abundance at or below those of benchmark $O_5F_{1.8}I_{0.2}$. Table 3 presents the five highest-ranked O_3I_4 and five highest-ranked O_5I_2 compositions, sorted by predicted iodine loading. These candidates represent promising directions for experimental validation, with the potential to substantially increase iodine immobilization while maintaining practical material cost and elemental abundance.

Trends Among Top Candidates

Analysis of the ten highest-ranked high-entropy pyrochlore candidates reveals consistent trends in *B*-site cation selection and their underlying rationale. Silicon is present in all ten candidate compositions—its small size and +4 oxidation state are likely to enable both charge balance and the structural accommodation of large iodide ions, highlighting its importance for stabilizing both O_3I_4 and O_5I_2 frameworks. For O_3I_4 candidates, aluminum appears in every case, which may help support charge balance at lower *B*-site charge requirements, and is entirely absent from the O_5I_2 group. In contrast, molybdenum is present in all O_5I_2 candidates and in two O_3I_4 candidates, while tungsten appears exclusively in O_5I_2; both appear to provide the higher *B*-site valence necessary for charge compensation in these stoichiometries.

Niobium is present in three out of five candidates in each group, and titanium is found in three O_3I_4 and two O_5I_2 candidates; their compatible oxidation states and ionic radii are expected to further promote pyrochlore stability. Other cations—including magnesium, manganese, antimony, and zirconium—are included only occasionally, appearing in no more than four of the top ten candidates, likely due to stricter requirements for charge balance, size, and overall phase stability.

An added benefit of these candidate compositions is the frequent inclusion of classic glass formers, silicon and aluminum.[142−144] Their presence could facilitate integration of high-entropy pyrochlore phases into glass-ceramic composite waste forms, which would be advantageous for processing flexibility and long-term immobilization of iodine-bearing nuclear waste.[145]

Future Directions

Further work should incorporate higher-fidelity stability metrics. While δ_χ and δ_r serve as practical, empirical screening tools, advanced descriptors such as the entropy forming ability[85] (EFA) and disordered enthalpy−entropy descriptor[146] (DEED) are based on density functional theory calculations. Unlike empirical methods—constructed using limited sets of known structures and thus carrying bias toward these compounds— EFA and DEED are first-principles descriptors, grounded in fundamental thermodynamics and quantum mechanics, making them broadly applicable to new and unexplored materials spaces. Since 2018, EFA and DEED have validated the formability of over 60 compositions and driven the discovery of 19 new high-entropy ceramics.[85,146,147] Although density functional theory calculations are demanding, machine learning now enables faster predictions and broader compositional screening.[97] These accelerated approaches are essential for high-entropy pyrochlore discovery, given the

https://doi.org/10.1021/prechem.5c00467
Precis. Chem. XXXX, XXX, XXX−XXX

much larger unit-cell size (22 atoms) relative to typical cubic-alloy and rocksalt structures (1−2 atoms per cell).

Expanding anion chemistry remains a key direction for future research. The pyrochlore structure accommodates seven anion sites, allowing for compositions that span from oxygen-rich (e.g., O_6I_1) to fully iodide-substituted (I_7). The existence of stable $A_2B_2F_7$ pyrochlores[148,149] motivates the search for $A_2B_2I_7$ analogues, which could maximize iodine loading in pyrochlores if suitable cation combinations can stabilize the structure. Exploring additional compositional degrees of freedom, such as *A*-site substitution and varying the number of species on either the *A*- or *B*-site, may increase configurational entropy and stability. These strategies must be balanced against potential reductions in iodine loading (by weight) and increased risk of site cross-mixing. Increasing compositional complexity continues to challenge the design of robust, thermodynamically stable phases.

Synthesizability remains to be established for these systems, and experimental validation will be essential to confirm phase stability, iodine uptake, and durability. To the best of our knowledge, halide-containing high-entropy pyrochlores have not yet been reported, highlighting the need to understand how halide incorporation influences synthesis. High-entropy oxide pyrochlores are typically prepared via solid−state reactions. However, the lower melting and boiling points of metal halide precursors[150] make them prone to volatilization at high temperatures, which can lead to compositional deviation. Moreover, substituting O^{2-} with halide anions introduces charge imbalance. Unless this is compensated by redesigning the composition, the system may accommodate the imbalance through vacancy formation or cation valence changes,[84] both of which may affect phase stability. Halides also differ substantially from oxygen in ionic size, electronegativity, and polarizability. These differences alter metal−anion bonding and local chemical environments, which can shift phase boundaries between pyrochlore and competing structures such as perovskite and fluorite. As a result, conventional criteria such as the radius ratio $r(A)/r(B)$[151] may be less reliable, underscoring the need for new descriptors that capture halide effects. The large size and high polarizability of iodide also introduce substantial challenges. In particular, iodide tends to form less rigid, more covalent bonds, which can increase lattice strain and instability at high incorporation levels. Hydrothermal methods can be advantageous for synthesizing iodide-rich pyrochlores, but their scope is limited by compositional complexity and the absence of established protocols for certain anion-rich variants, such as O_6F pyrochlores. These compositions often require complex cation chemistries to maintain charge balance, which further complicates synthesis. Other methods—including solid−state reaction, high-temperature and high-pressure synthesis, spark plasma sintering, microwave-assisted approaches, and solvothermal methods—also have distinct advantages and limitations.[34] Additional effort will therefore be required to identify and optimize the most suitable synthesis route for iodide-rich pyrochlores.

Combining high-throughput computation, machine learning models for EFA and DEED for these compositions, and targeted experiments will be key to realizing high-entropy ceramics for efficient and sustainable iodine immobilization in nuclear waste forms.

CONCLUSION

In this work, we demonstrate that iodine can be successfully incorporated into the pyrochlore structure using a known oxyfluoride pyrochlore as the starting material. This is the first experimental observation of an iodine-containing pyrochlore. SEM confirms the preservation of pyrochlore morphology after iodine incorporation, while XRD reveals lattice expansion at low iodide content and contraction as excess iodide leads to vacancy formation. Raman spectroscopy and XPS support a model in which iodide incorporation induces local lattice distortion, with a solubility limit beyond which further iodide uptake is not possible.

To overcome these intrinsic limits and enable higher iodine loading, we adopted a high-entropy design strategy. Previous studies have shown that anion sublattices in high-entropy ceramics can accommodate local distortions induced by multiple cation species. In contrast, our approach leverages cation diversity to potentially stabilize phases with substantial lattice distortions localized in the anion sublattice—directly addressing the challenge of incorporating large iodide ions. Computational screening of over 40,000 candidate compositions indicates that high-entropy pyrochlores could, in principle, achieve iodine loadings up to 74 wt %, while also reducing material costs and improving resource security. The high-entropy candidates identified here achieve a minimum iodine loading of 33 wt %, surpassing most existing ceramic waste forms and underscoring the value of this design space. The resulting design landscape reveals clear chemical trends driven by charge balance and cation size, and can be further optimized with criteria such as glass-former compatibility.

Together, experimental and computational insights suggest that only a narrow compositional space holds promise for stable, highly iodine-loaded, and economically feasible pyrochlores, highlighting the importance of data-driven approaches for new nuclear waste form design. Synthesis and experimental validation of high-entropy candidates is essential. If realized, high-entropy iodine-pyrochlores could offer a robust, scalable, and cost-effective platform for long-term containment of iodine-bearing nuclear waste.

METHODS

Experimental Design

We performed a series of hydrothermal experiments, systematically varying the iodine-to-fluorine ionic ratio in solution to probe iodide incorporation in the pyrochlore structure. The oxyfluoride pyrochlore $Na_2Nb_2O_5F_2$ was selected as the base composition for substitution studies. For clarity, sample annotations omit Na and Nb, labeling only the *X*- and *X*′-site anions, as also noted in the figure captions. All sample names directly reflect their nominal stoichiometries. Seven compositions were synthesized with different fluoride/iodide ratios: O_5F_2, $O_5F_{1.9}I_{0.1}$, $O_5F_{1.8}I_{0.2}$, $O_5F_{1.7}I_{0.3}$, $O_5F_1I_1$, $O_5F_{0.5}I_{1.5}$, and O_5I_2. The sample naming scheme is summarized in Table 1.

Materials Synthesis

Sodium fluoride (NaF) was purchased from Fisher Scientific. Niobium pentoxide (Nb_2O_5) and sodium iodide (NaI) were obtained from Thermo Scientific. Samples were prepared by a hydrothermal method.[18] For $Na_2Nb_2O_5F_2$, a 2 M aqueous solution of NaF was prepared with deionized water (4 mL), to which 0.004 mol (1.0632 g) Nb_2O_5 was added. After 30 min ultrasonication, the mixture was transferred to a polytetrafluoroethylene vessel, sealed in a stainless-steel autoclave, and heated at 220 °C for 60 h. After cooling, the product was collected, washed twice with deionized water, centrifuged, rinsed once with ethanol, and dried overnight at 60 °C.

https://doi.org/10.1021/prechem.5c00467
Precis. Chem. XXXX, XXX, XXX−XXX

Iodine-containing pyrochlores were synthesized using precursor solutions in which NaF was partially replaced by NaI according to the nominal stoichiometry. Prior to hydrothermal treatment, solutions were purged with Ar to minimize oxidation and then processed as above.

Materials Characterization

X-ray diffraction (XRD) was performed using a Malvern Panalytical Aeris powder diffractometer (40 kV, 7.5 mA) with Cu Kα radiation (λ = 1.5406 Å). Rietveld refinements were carried out using GSAS-II.[152] Scanning electron microscopy (SEM) and energy dispersive X-ray spectroscopy (EDS) were conducted on a JEOL IT700H SEM equipped with an EDAX Octane Elect EDS/EDX System. A 5−10 nm carbon layer was deposited on all ceramic powder samples using a Leica EM ACE200 sputter coater before SEM observation. Raman spectroscopy was performed on a Horiba LabRAM HR Evolution confocal Raman microscope with a 532 nm continuous-wave excitation source. X-ray photoelectron spectroscopy (XPS) was performed using a PHI 5600 instrument with a Mg Kα X-ray source. XPS depth profiling, which involves sequential sputtering and analysis to obtain subsurface chemical information, was not performed. This approach is not well suited to powder samples, as surface roughness reduces depth resolution and preferential sputtering and chemical reduction during the process can further alter the chemical profile and complicate interpretation.[153−155] Therefore, we focused on surface-sensitive XPS measurements, which provide more reliable and meaningful results for powdered ceramic specimens.

Leaching Test

The dissolution behavior of the $O_5F_{1.7}I_{0.3}$ sample was examined using a powder-based static leaching protocol adapted from the ASTM C1285 Product Consistency Test[96,156,157] and modified for accelerated hydrothermal conditions. The specific surface area of the powder fraction was determined using the Brunauer−Emmett−Teller method. The powder was then transferred into polytetrafluoroethylene (Teflon) vessels containing deionized water, with a liquid-to-solid ratio of 10 mL g^{-1}. The vessels were sealed within airtight stainless-steel autoclaves and heated in an oven at 150 °C for 3 days. At selected time intervals, the leachate solution was collected. The elemental concentrations in the filtered solutions were quantified by ion chromatography (Dionex ICS-6000 HPIC). The normalized leaching rate (r) of iodine was calculated in units of g m^{-2} d^{-1} according to

$$r = \frac{C}{t \times f \times (S/V)} \quad (1)$$

where C (g L^{-1}) is the concentration of iodine in water after leaching time t (day), S/V (m^2 L^{-1}) is the specific surface area of the sample divided by the volume of the leachate, and f is the mass fraction of iodine in the sample.

Analysis of High-Entropy Design

Twenty-nine reported *B*-site elements with oxidation states from +2 to +6 were selected as candidates for high-entropy iodine-containing pyrochlores, and all combinatorial chemical compositions with five equimolar *B*-site elements satisfying charge neutrality were generated. Iodine loading was calculated as the total atomic mass of iodine divided by the total atomic mass of all elements in the composition, weighted by their proportions. Economic descriptors, including crustal abundance and elemental price, were taken from the `mendeleev` Python library;[141] missing data were filled using the median value of each data set. Compositions containing Tc, Ru, Rh, Re, Os, Ir, or Pt were excluded from price and abundance analyses due to rarity or radioactivity. Price and abundance results report the weighted average for *B*-site elements only, excluding Na, O, and I.

■ ASSOCIATED CONTENT

Supporting Information

The Supporting Information is available free of charge at https://pubs.acs.org/doi/10.1021/prechem.5c00467.

Supporting Information contains the Rietveld refinement of the XRD data, XPS spectrum, EDS mapping, and leaching test results (PDF)

■ AUTHOR INFORMATION

Corresponding Author

Corey Oses − *Department of Materials Science and Engineering, Johns Hopkins University, Baltimore, Maryland 21218, United States; Johns Hopkins Data Science and AI Institute, Ralph O'Connor Sustainable Energy Institute, and William H. Miller III Department of Physics and Astronomy, Johns Hopkins University, Baltimore, Maryland 21218, United States;* orcid.org/0000-0002-3790-1377; Email: corey@jhu.edu

Authors

Xiao Xu − *Department of Materials Science and Engineering, Johns Hopkins University, Baltimore, Maryland 21218, United States; Johns Hopkins Data Science and AI Institute, Johns Hopkins University, Baltimore, Maryland 21218, United States;* orcid.org/0009-0008-4118-4746

Guangshuai Han − *Department of Materials Science and Engineering, Johns Hopkins University, Baltimore, Maryland 21218, United States; Johns Hopkins Data Science and AI Institute and Ralph O'Connor Sustainable Energy Institute, Johns Hopkins University, Baltimore, Maryland 21218, United States*

Tianhao Li − *Department of Materials Science and Engineering, Johns Hopkins University, Baltimore, Maryland 21218, United States; Johns Hopkins Data Science and AI Institute, Johns Hopkins University, Baltimore, Maryland 21218, United States;* orcid.org/0009-0006-2035-7754

Jiayue Hu − *Department of Materials Science and Engineering, Johns Hopkins University, Baltimore, Maryland 21218, United States; Johns Hopkins Data Science and AI Institute and Ralph O'Connor Sustainable Energy Institute, Johns Hopkins University, Baltimore, Maryland 21218, United States*

Guotao Qiu − *Department of Materials Science and Engineering, Johns Hopkins University, Baltimore, Maryland 21218, United States*

Shao-Yu Tseng − *Department of Materials Science and Engineering, Johns Hopkins University, Baltimore, Maryland 21218, United States*

Gyeong Ho Han − *Department of Materials Science and Engineering, University of Pennsylvania, Philadelphia, Pennsylvania 19104, United States*

Alexander D. Dupuy − *Department of Materials Science and Engineering, University of Connecticut, Storrs, Connecticut 06268, United States*

Anthony Shoji Hall − *Department of Materials Science and Engineering, Johns Hopkins University, Baltimore, Maryland 21218, United States; Department of Materials Science and Engineering, University of Pennsylvania, Philadelphia, Pennsylvania 19104, United States;* orcid.org/0000-0003-4134-4160

Complete contact information is available at: https://pubs.acs.org/10.1021/prechem.5c00467

Notes

The authors declare no competing financial interest.

https://doi.org/10.1021/prechem.5c00467
Precis. Chem. XXXX, XXX, XXX−XXX

■ ACKNOWLEDGMENTS

The authors thank Robert Ledoux (ARPA-E), Assel Aitkaliyeva (ARPA-E), Jeremiah Beam (ARPA-E), Anil Ganti (ARPA-E), Jonathan Melville (ARPA-E), Bill McNamara (JHU), A.J. Donelson (JHU), Chip Cotton (JHU), S.M. Koohpayeh (JHU), and Jie Lian (RPI) for helpful discussions. Research was sponsored by the Advanced Research Projects Agency-Energy (ARPA-E) (DE-AR0001787). X.X. acknowledges support from the Institute for Data-Intensive Engineering and Science (IDIES) at JHU. T.L. and G.Q. acknowledge support from the Ralph O'Connor Sustainable Energy Institute (ROSEI) at JHU. C.O. acknowledges the computational resources provided by the Advanced Research Computing at Hopkins (ARCH), which is supported by the National Science Foundation (NSF) Grant (OAC1920103), and the Texas Advanced Computing Center (TACC) at The University of Texas at Austin.

■ REFERENCES

(1) Parker, C., Smarter waste strategies: Helping deliver on the promise of advanced nuclear, https://www.ans.org/news/2025-06-06/article-7044/smarter-waste-strategies-helping-deliver-on-the-promise-of-advanced-nuclear/ 2025 (accessed Dec 5, 2025).
(2) Alsudairy, Z.; Brown, N.; Yang, C.; Cai, S.; Akram, F.; Ambus, A.; Ingram, C.; Li, X. Facile microwave-assisted synthesis of 2D imine-linked covalent organic frameworks for exceptional iodine capture. *Precis. Chem.* **2023**, *1*, 233−240.
(3) Asmussen, R. M.; Turner, J.; Chong, S.; Riley, B. J. Review of recent developments in iodine wasteform production. *Front. Chem.* **2022**, *10*, 1043653.
(4) Chao, J. H.; Tseng, C. L.; Lee, C. J.; Hsia, C. C.; Teng, S. P. Analysis of I-129 in radwastes by neutron activation. *Appl. Radiat. Isot.* **1999**, *51*, 137−143.
(5) Wainwright, H. M.; Whiteaker, K.; Gonzalez-Raymat, H.; Denham, M. E.; Pegg, I. L.; Kaplan, D. I.; Qafoku, N. P.; Wilson, D.; Wilson, S.; Eddy-Dilek, C. A. The iodine-129 paradox in nuclear waste management strategies. *Nat. Sustain.* **2025**, *8*, 1391−1399.
(6) Zhang, S.; Schwehr, K. A.; Ho, Y.-F.; Xu, C.; Roberts, K. A.; Kaplan, D. I.; Brinkmeyer, R.; Yeager, C. M.; Santschi, P. H. A novel approach for the simultaneous determination of iodide, iodate and organo-iodide for ^{127}I and ^{129}I in environmental samples using gas chromatography-mass spectrometry. *Environ. Sci. Technol.* **2010**, *44*, 9042−9048.
(7) Chao, J.-H.; Tseng, C.-L. ^{129}I concentrations of mammalian thyroids in Taiwan. *Sci. Total Environ.* **1996**, *193*, 111−119.
(8) OECD Nuclear Energy Agency, Management of Recyclable Fissile and Fertile Materials, Tech. Rep., OECD Nuclear Energy Agency (2007). https://www.oecd-nea.org/upload/docs/application/pdf/2019-12/6107-manage-recyclable.pdf accessed Dec 25, 2025.
(9) Yusubov, M. S.; Zhdankin, V. V. Iodine catalysis: A green alternative to transition metals in organic chemistry and technology. *Resour. -Effic. Technol.* **2015**, *1*, 49−67.
(10) Hyatt, N. C.; Ojovan, M. I. Materials for nuclear waste immobilization. *Materials* **2019**, *12*, 3611.
(11) Zhu, H.; Wang, F.; Liao, Q.; Zhu, Y. Synthesis and characterization of zirconolite-sodium borosilicate glass-ceramics for nuclear waste immobilization. *J. Nucl. Mater.* **2020**, *532*, 152026.
(12) Zhang, Y.; Kong, L.; Ionescu, M.; Gregg, D. J. Current advances on titanate glass-ceramic composite materials as waste forms for actinide immobilization: A technical review. *J. Eur. Ceram. Soc.* **2022**, *42*, 1852−1876.
(13) Zhang, Y.; Zhang, Z.; Thorogood, G.; Vance, E. R. Pyrochlore based glass-ceramics for the immobilization of actinide-rich nuclear wastes: From concept to reality. *J. Nucl. Mater.* **2013**, *432*, 545−547.
(14) Xie, H.; Feng, Z.; Wang, L. Effects of pyrochlore content on the phase, structure, and properties of uranium-rich glass ceramics. *Ceram. Int.* **2020**, *46*, 13549−13555.
(15) Ewing, R. C.; Weber, W. J.; Lian, J. Nuclear waste disposal−Pyrochlore ($A_2B_2O_7$): Nuclear waste form for the immobilization of plutonium and "minor" actinides. *J. Appl. Phys.* **2004**, *95*, 5949−5971.
(16) Feng, Z.; Xie, H.; Wang, L.; Deng, S.; Li, J. Glass-ceramics with internally crystallized pyrochlore for the immobilization of uranium wastes. *Ceram. Int.* **2019**, *45*, 16999−17005.
(17) McCloy, J. S.; Goel, A. Glass-ceramics for nuclear-waste immobilization. *MRS Bull.* **2017**, *42*, 233−240.
(18) Boivin, E.; Pourpoint, F.; Saitzek, S.; Simon, P.; Roussel, P.; Kabbour, H. An unusual O^{2-}/F^{-} distribution in the new pyrochlore oxyfluorides: $Na_2B_2O_5F_2$ (B= Nb, Ta). *Chem. Commun.* **2022**, *58*, 2391−2394.
(19) Chen, X.; Pang, R.; Wang, S.; Yuan, W.; Su, J.; Tan, T.; Zhang, S.; Li, C.; Zhang, H. Sunlight-activated Eu^{3+}-doped $CaNaSb_2O_6F$ yellow-orange long-persistence luminescence material. *Inorg. Chem. Front.* **2023**, *10*, 2926−2938.
(20) Yang, K.; Zhu, W.; Scott, S.; Wang, Y.; Wang, J.; Riley, B. J.; Vienna, J.; Lian, J. Immobilization of cesium and iodine into $Cs_3Bi_2I_9$ perovskite-silica composites and core-shell waste forms with high waste loadings and chemical durability. *J. Hazard. Mater.* **2021**, *401*, 123279.
(21) Sun, Q.; Xu, Y.; Zhang, H.; Xiao, B.; Liu, X.; Dong, J.; Cheng, Y.; Zhang, B.; Jie, W.; Kanatzidis, M. G. Optical and electronic anisotropies in perovskitoid crystals of $Cs_3Bi_2I_9$ studies of nuclear radiation detection. *J. Mater. Chem. A* **2018**, *6*, 23388−23395.
(22) Uno, M.; Shinohara, M.; Kurosaki, K.; Yamanaka, S. Some properties of a lead vanado-iodoapatite $Pb_{10}(VO_4)_6$ I_2. *J. Nucl. Mater.* **2001**, *294*, 119−122.
(23) Talanov, M. V.; Talanov, V. M. Structural diversity of ordered pyrochlores. *Chem. Mater.* **2021**, *33*, 2706−2725.
(24) Chakoumakos, B. C. Systematics of the pyrochlore structure type, ideal $A_2B_2X_6Y$. *J. Solid State Chem.* **1984**, *53*, 120−129.
(25) Lian, J.; Wang, L.; Chen, J.; Sun, K.; Ewing, R. C.; Matt Farmer, J.; Boatner, L. A. The order−disorder transition in ion-irradiated pyrochlore. *Acta Mater.* **2003**, *51*, 1493−1502.
(26) Subramanian, M. A.; Aravamudan, G.; Subba Rao, G. V. Oxide pyrochlores — A review. *Prog. Solid State Chem.* **1983**, *15* (2), 55−143.
(27) Xu, J.; Xi, R.; Xu, X.; Zhang, Y.; Feng, X.; Fang, X.; Wang, X. $A_2B_2O_7$ pyrochlore compounds: a category of potential materials for clean energy and environment protection catalysis. *J. Rare Earths* **2020**, *38*, 840−849.
(28) Fujinaka, H.; Kinomura, N.; Koizumi, M.; Miyamoto, Y.; Kume, S. Syntheses and physical properties of pyrochlore-type $A_2B_2O_7$ (A = Tl, Y; B = Cr, Mn). *Mater. Res. Bull.* **1979**, *14*, 1133−1137.
(29) Wan, C.; Qu, Z.; Du, A.; Pan, W. Influence of B site substituent Ti on the structure and thermophysical properties of $A_2B_2O_7$-type pyrochlore $Gd_2Zr_2O_7$. *Acta Mater.* **2009**, *57*, 4782−4789.
(30) Martínez-Lope, M. J.; Casais, M. T.; Alonso, J. A. Synthesis and characterization of the oxynitride $Y_2Mo_2O_{4.5}N_{2.5}$ pyrochlore: A neutron diffraction and magnetic study. *Z. Naturforsch. B:Chem. Sci.* **2006**, *61*, 164−169.
(31) Bernard, D.; Lucas, J.; Rivoallan, L. Les pyrochlores ferroelectriques derives de $Cd_2Nb_2O_6S$: Mise en évidence des transitions de phase par des techniques d'optique non linéaire. *Solid State Commun.* **1976**, *18*, 927−930.
(32) Phraewphiphat, T.; Iqbal, M.; Suzuki, K.; Hirayama, M.; Kanno, R. Synthesis and lithium-ion conductivity of $LiSrB_2O_6F$ (B = Nb^{5+}, Ta^{5+}) with a pyrochlore structure. *J. Jpn. Soc. Powder Powder Metall.* **2018**, *65*, 26−33.
(33) Fuentes, A. F.; O'Quinn, E. C.; Montemayor, S. M.; Zhou, H.; Lang, M.; Ewing, R. C. Pyrochlore-type lanthanide titanates and zirconates: Synthesis, structural peculiarities, and properties. *Appl. Phys. Rev.* **2024**, *11*, 021337.
(34) Qiu, G.; Li, T.; Xu, X.; Liu, Y.; Niyogi, M.; Cariaga, K.; Oses, C. High Entropy Powering Green Energy: Hydrogen, Batteries, Electronics, and Catalysis. *npj Comput. Mater.* **2025**, *11*, 145.

https://doi.org/10.1021/prechem.5c00467
Precis. Chem. XXXX, XXX, XXX−XXX

(35) Xu, C.; Xiao, X.; Cai, C.; Cheng, Q.; Zhu, L.; Zhang, J.; Wei, B.; Wang, H. Insight into the differences in carbon dots prepared from fish scales using conventional hydrothermal and microwave methods. *Environ. Sci. Pollut. Res.* **2023**, *30*, 54616−54627.
(36) Zhang, S.; Xiang, L.; Liu, Y.; Feng, Y.; Zhang, Y. Hydrothermal-based synthesis of iodosodalite waste forms to immobilize iodine eluent. *J. Radioanal. Nucl. Chem.* **2024**, *333*, 4705−4714.
(37) Li, S.; Xu, Q.; Uchaker, E.; Cao, X.; Cao, G. Comparison of amorphous, pseudohexagonal and orthorhombic Nb_2O_5 for high-rate lithium ion insertion. *CrystEngComm* **2016**, *18*, 2532−2540.
(38) Hardy, J. S.; Templeton, J. W.; Edwards, D. J.; Lu, Z.; Stevenson, J. W. Lattice expansion of LSCF-6428 cathodes measured by in situ XRD during SOFC operation. *J. Power Sources* **2012**, *198*, 76−82.
(39) Liu, D.; Li, G.; Dang, P.; Zhang, Q.; Wei, Y.; Lian, H.; Shang, M.; Lin, C. C.; Lin, J. Simultaneous broadening and enhancement of Cr^{3+} photoluminescence in $LiIn_2SbO_6$ by chemical unit cosubstitution: night-vision and near-infrared spectroscopy detection applications. *Angew. Chem., Int. Ed.* **2021**, *60*, 14644−14649.
(40) Zaitsev, A. N.; Spratt, J.; Shtukenberg, A. G.; Zolotarev, A. A.; Britvin, S. N.; Petrov, S. V.; Kuptsova, A. V.; Antonov, A. V. Oscillatory-and sector-zoned pyrochlore from carbonatites of the Kerimasi volcano, Gregory rift, Tanzania. *Mineral. Mag.* **2021**, *85*, 532−553.
(41) Yoo, C.-Y.; Kim, J.; Kim, S.-C.; Kim, S.-J. Crystal structures of new layered perovskite-type oxyfluorides, $CsANb_2O_6F$ (A = Sr and Ca) and comparison with pyrochlore-type $CsNb_2O_5F$. *J. Solid State Chem.* **2018**, *267*, 146−152.
(42) Vandenborre, M. T.; Husson, E.; Fourquet, J. L. Etude spectroscopique par absorption infra-rouge et diffusion Raman de composes oxyfluores de structure pyrochlore ANb_2O_5F (A = Rb, Cs, Tl) et $RbTa_2O_5F$. *Mater. Res. Bull.* **1982**, *17*, 1359−1364.
(43) Liu, X.; Zhang, P.; Huang, M.; Han, Y.; Xu, N.; Li, Y.; Zhang, Z.; Pan, W.; Wan, C. Effect of lattice distortion in high-entropy $RE_2Si_2O_7$ and RE_2SiO_5 (RE = Ho, Er, Y, Yb, and Sc) on their thermal conductivity: Experimental and molecular dynamic simulation study. *J. Eur. Ceram. Soc.* **2023**, *43*, 6407−6415.
(44) Liarokapis, E.; Leventouri, T.; Lampakis, D.; Palles, D.; Neumeier, J. J.; Goodwin, D. H. Local lattice distortions and Raman spectra in the $La_{1-x}Ca_xMnO_3$ system. *Phys. Rev. B* **1999**, *60*, 12758.
(45) Shuker, R.; Gammon, R. W. Raman-scattering selection-rule breaking and the density of states in amorphous materials. *Phys. Rev. Lett.* **1970**, *25*, 222.
(46) Nguyen, T. H.; Nguyen, T. M. H.; Kang, B.; Cho, B.; Han, M.; Choi, H. J.; Kong, M.; Lee, Y.; Yang, I.-S. Raman spectroscopic evidence of impurity-induced structural distortion in SmB_6. *J. Raman Spectrosc.* **2019**, *50*, 1661−1671.
(47) Jin, Y.; Cui, Q.; Wen, G.; Wang, Q.; Hao, J.; Wang, S.; Zhang, J. XPS and Raman scattering studies of room temperature ferromagnetic ZnO: Cu. *J. Phys. D: Appl. Phys.* **2009**, *42*, 215007.
(48) Hao, L.; Huang, H.; Zhang, Y.; Ma, T. Oxygen vacant semiconductor photocatalysts. *Adv. Funct. Mater.* **2021**, *31*, 2100919.
(49) Santara, B.; Giri, P. K.; Imakita, K.; Fujii, M. Microscopic origin of lattice contraction and expansion in undoped rutile TiO_2 nanostructures. *J. Phys. D: Appl. Phys.* **2014**, *47*, 215302.
(50) Nekipelov, S. V.; Petrova, O. V.; Koroleva, A. V.; Krzhizhanovskaya, M. G.; Zhuk, N. A. XPS study of pyrochlore type $Bi_2Cu_{1/3}Ni_{1/3}Co_{1/3}M_2O_{9\pm\delta}$ (M-Nb,Ta). *Ceram. Int.* **2025**, *51*, 3343−3349.
(51) Feng, Q.; Zhang, Z.; Huang, H.; Yao, K.; Fan, J.; Zeng, L.; Williams, M. C.; Li, H.; Wang, H. An effective strategy to tune the oxygen vacancy of pyrochlore oxides for electrochemical energy storage and conversion systems. *Chem. Eng. J.* **2020**, *395*, 124428.
(52) Escamilla, R.; López Aranda, J. A.; Cervantes, J. M.; Muñoz, H.; León-Flores, J.; Antonio, J. E.; Pilo, J.; Arévalo López, E. P.; Romero, M. Molten salts synthesis and Raman, XPS, and UV−vis spectroscopy study of Zn-doped $Y_2Ti_2O_{7-\delta}$ pyrochlore. *Ceram. Int.* **2024**, *50*, 15944−15951.
(53) Injac, S. D.; Mullens, B. G.; Denis Romero, F.; Avdeev, M.; Barnett, C.; Yuen, A. K. L.; Amano Patino, M.; Mukherjee, S.; Vaitheeswaran, G.; Singh, D. J.; Kennedy, B. J.; Shimakawa, Y. Characterisation of $Pb_2Rh_2O_7$ and $Y_2Rh_2O_7$: an unusual case of pyrochlore stabilisation under high pressure, high temperature synthesis conditions. *J. Mater. Chem. C* **2024**, *12*, 3077−3089.
(54) Dey, M.; Bhattacharjee, S.; Chakrabarty, A.; Mitchell, R. H.; Pal, S.; Pal, S.; Sen, A. K. Compositional variation and genesis of pyrochlore, belkovite and baotite from the Sevattur carbonatite complex, India. *Mineral. Mag.* **2021**, *85*, 588−606.
(55) Yin, R.; Sun, X.; Wang, S.; Wu, B. Mineral Chemistry of Pyrochlore Supergroup Minerals as Records of Nb Mineralization Processes in NYF-Type Pegmatites: A Case Study of the Emeishan Large Igneous Province, SW China. *Minerals* **2024**, *14*, 13.
(56) Oka, K.; Hojo, H.; Azuma, M.; Oh-Ishi, K. Temperature-independent, large dielectric constant induced by vacancy and partial anion order in the Oxyfluoride Pyrochlore $Pb_2Ti_2O_{6-\delta}F_{2\delta}$. *Chem. Mater.* **2016**, *28*, 5554−5559.
(57) Fan, L.; Shen, H.; Ji, D.; Xing, Y.; Tao, L.; Sun, Q.; Guo, S. Biaxially compressive strain in Ni/Ru core/shell nanoplates boosts $Li-CO_2$ batteries. *Adv. Mater.* **2022**, *34*, 2204134.
(58) Hassan, M. u.; Venkatesan, S.; Ryu, H. J. Non-volatile immobilization of iodine by the cold-sintering of iodosodalite. *J. Hazard. Mater.* **2020**, *386*, 121646.
(59) Yang, K.; Wang, Y.; Shen, J.; Scott, S. M.; Riley, B. J.; Vienna, J. D.; Lian, J. $Cs_3Bi_2I_9$-hydroxyapatite composite waste forms for cesium and iodine immobilization. *J. Adv. Ceram.* **2022**, *11*, 712−728.
(60) Lere-Adams, A. J.; Wilkins, M. C. D.; Bollinger, D.; Stariha, S.; Farzana, R.; Dayal, P.; Gregg, D. J.; Chong, S.; Riley, B. J.; Heiden, Z. M.; McCloy, J. S. Glass-bonded ceramic waste forms for immobilization of radioiodine from caustic scrubber wastes. *J. Nucl. Mater.* **2024**, *591*, 154938.
(61) Liu, Y.; Feng, Y.; Wei, G.; Sun, R.; Lu, X.; Chen, Y.; Peng, L.; Ma, M.; Zhang, Y.; Zhang, Z. Synthesis of glass composite material with bismuthate glass powder and zeolite-4A for immobilization of iodine waste. *J. Solid State Chem.* **2021**, *294*, 121856.
(62) Pitike, K. C.; Macias, A.; Eisenbach, M.; Bridges, C. A.; Cooper, V. R. Computationally accelerated discovery of high entropy pyrochlore oxides. *Chem. Mater.* **2022**, *34*, 1459−1472.
(63) Wright, A. J.; Wang, Q.; Ko, S.-T.; Chung, K. M.; Chen, R.; Luo, J. Size disorder as a descriptor for predicting reduced thermal conductivity in medium- and high-entropy pyrochlore oxides. *Scr. Mater.* **2020**, *181*, 76−81.
(64) Jia, H.; Li, C.; Chen, G.; Li, H.; Li, S.; An, L.; Chen, K. Design and synthesis of high-entropy pyrochlore ceramics based on valence combination. *J. Eur. Ceram. Soc.* **2022**, *42*, 5973−5983.
(65) Li, Y.; Lei, Y.; Zhao, S.; Xiao, H.; Liu, H.; Wang, Y.; Luo, Y.; Zhang, J.; Wang, J.; Ewing, R. C.; Wang, C. Phase transformation and radiation resistance of B-site high entropy pyrochlores. *Scr. Mater.* **2023**, *229*, 115367.
(66) Teng, Z.; Tan, Y.; Zeng, S.; Meng, Y.; Chen, C.; Han, X.; Zhang, H. Preparation and phase evolution of high-entropy oxides $A_2B_2O_7$ with multiple elements at A and B sites. *J. Eur. Ceram. Soc.* **2021**, *41*, 3614−3620.
(67) Vayer, F.; Decorse, C.; Bérardan, D.; Dragoe, D.; Dragoe, N. Investigation of the chemical versatility in high-entropy pyrochlores. *J. Am. Ceram. Soc.* **2023**, *106*, 2601.
(68) Wang, H.; Zhu, C.; Wang, Z.; Wang, M.; Li, Y. Mechanical property and irradiation resistance of high entropy pyrochlore $(Sm_{0.2}Eu_{0.2}Gd_{0.2}Y_{0.2}Lu_{0.2})_2$ Ti_2O_7. *Nucl. Instrum. Methods Phys. Res.* **2022**, *533*, 17−22.
(69) Wang, Z.; Zhu, C.; Wang, H.; Wang, M.; Liu, C.; Yang, D.; Li, Y. Preparation and irradiation stability of $A_2B_2O_7$ pyrochlore high-entropy ceramic for immobilization of high-level nuclear waste. *J. Nucl. Mater.* **2023**, *574*, 154212.
(70) Vayer, F.; Decorse, C.; Bérardan, D.; Dragoe, N. New entropy-stabilized oxide with pyrochlore structure: $Dy_2(Ti_{0.2}Zr_{0.2}Hf_{0.2}Ge_{0.2}Sn_{0.2})_2$ O_7. *J. Alloys Compd.* **2021**, *883*, 160773.

https://doi.org/10.1021/prechem.5c00467
Precis. Chem. XXXX, XXX, XXX−XXX

(71) Jia, H.; Li, C.; Chen, G.; Gong, B.; Li, S.; Zhou, Y.; An, L.; Chen, K. Design, synthesis, and influencing factors of medium-/high-entropy $Y_2(ZrTiGeHfSnSi)_2$ O_7 with a pyrochlore structure. *J. Eur. Ceram. Soc.* **2024**, *44*, 3296−3306.
(72) Liu, H.-L.; Pang, S.; Liu, C.-Q.; Wu, Y.-T.; Zhang, G.-J. High-entropy yttrium pyrochlore ceramics with glass-like thermal conductivity for thermal barrier coating application. *J. Am. Ceram. Soc.* **2022**, *105*, 6437−6448.
(73) Li, Y.; Lei, Y.; Xiao, H.; Zhao, S.; Wang, Y.; Cao, Z.; Zhang, J.; Wang, J.; Lu, G.; Cao, L.; Wang, C. Different mechanisms of A-site and B-site high entropy effect on radiation tolerance of pyrochlores. *J. Mater. Sci. Technol.* **2024**, *191*, 250−258.
(74) Jia, H.; Li, C.; Chen, G.; Gong, B.; An, L.; Chen, K. Thermodynamic calculation, preparation and properties of $Y_2(Zr_{1/6}Ti_{1/3}Ge_{1/6}Hf_{1/12}Sn_{1/4})_2$ O_7 high-entropy pyrochlore ceramics. *Ceram. Int.* **2024**, *50*, 22671−22678.
(75) Xu, L.; Su, L.; Wang, H.; Gao, H.; Guo, P.; Niu, M.; Peng, K.; Zhuang, L.; Dai, Z. High-entropy $Sm_2B_2O_7$ (B = Ti, Zr, Sn, Hf, Y, Yb, Nb, and Ta) oxides with highly disordered B-site cations for ultralow thermal conductivity. *J. Mater. Sci. Technol.* **2022**, *119*, 182−189.
(76) Wang, Y.; Zhu, J.; Shao, G.; Wang, H.; Li, M.; Lu, H.; Zhang, R. Synthesis of high-entropy $La_2B_2O_7$ ceramics with non-equivalent principal elements in B-sites and their CMAS resistance performance. *J. Alloys Compd.* **2022**, *924*, 166635.
(77) Sickafus, K. E.; Grimes, R. W.; Valdez, J. A.; Cleave, A.; Tang, M.; Ishimaru, M.; Corish, S. M.; Stanek, C. R.; Uberuaga, B. P. Radiation-induced amorphization resistance and radiation tolerance in structurally related oxides. *Nat. Mater.* **2007**, *6*, 217−223.
(78) Stefanovsky, S. V.; Yudintsev, S. V.; Gieré, R.; Lumpkin, G. R. Nuclear waste forms. *Geol. Soc. Spec. Publ.* **2004**, *236*, 37−63.
(79) Li, H.; Xia, Y.; Xu, M.; Yi, M.; Zhao, C.; Wang, H.; Li, C.; Liu, L.; Watabe, H.; Li, Y. Study on structure and irradiation effects of Ln_3NbO_7 rare-earth niobate ceramics. *Ceram. Int.* **2025**, *51*, 38660−38669.
(80) Devarajan, Y.; Thiagarajan, C. Innovative materials for enhancing safety, efficiency, and sustainability in nuclear waste management. *Kerntechnik* **2025**, *90*, 261−274.
(81) Lian, J.; Helean, K. B.; Kennedy, B. J.; Wang, L. M.; Navrotsky, A.; Ewing, R. C. Effect of structure and thermodynamic stability on the response of lanthanide stannate pyrochlores to ion beam irradiation. *J. Phys. Chem. B* **2006**, *110*, 2343−2350.
(82) Wang, Y.; Jing, C.; Ding, Z.-Y.; Zhang, Y.-Z.; Wei, T.; Ouyang, J.-H.; Liu, Z.-G.; Wang, Y.-J.; Wang, Y.-M. The structure, property, and ion irradiation effects of pyrochlores: a comprehensive review. *Crystals* **2023**, *13*, 143.
(83) Elsherbeny, A. M.; Abdelghany, A. M.; Ghorab, S. M.; Shalaby, R. M. Investigating the impact of Nb_2O_5 on structural and shielding properties of aluminum fluorosilicate glass systems. *Radiat. Phys. Chem.* **2025**, *235*, 112824.
(84) Oses, C.; Toher, C.; Curtarolo, S. High-entropy ceramics. *Nat. Rev. Mater.* **2020**, *5*, 295−309.
(85) Sarker, P.; Harrington, T.; Toher, C.; Oses, C.; Samiee, M.; Maria, J.-P.; Brenner, D. W.; Vecchio, K. S.; Curtarolo, S. High-entropy high-hardness metal carbides discovered by entropy descriptors. *Nat. Commun.* **2018**, *9* (1), 4980.
(86) Oses, C.; Li, T.; Xu, X.; Han, G.; Qiu, G.; Owens, J. R. Beyond the four core effects: revisiting thermoelectrics with a high-entropy design. *Mater. Horiz.* **2025**, *12*, 5946−5956.
(87) Rost, C. M.; Rák, Z.; Brenner, D. W.; Maria, J.-P. Local structure of the $Mg_xNi_xCo_xCu_xZn_xO$(x = 0.2) entropy-stabilized oxide: An EXAFS study. *J. Am. Ceram. Soc.* **2017**, *100* (6), 2732−2738.
(88) Esters, M.; Oses, C.; Hicks, D.; Mehl, M. J.; Jahnátek, M.; Hossain, M. D.; Maria, J.-P.; Brenner, D. W.; Toher, C.; Curtarolo, S. Settling the matter of the role of vibrations in the stability of high-entropy carbides. *Nat. Commun.* **2021**, *12*, 5747.
(89) Braun, J. L.; Rost, C. M.; Lim, M.; Giri, A.; Olson, D. H.; Kotsonis, G. N.; Stan, G.; Brenner, D. W.; Maria, J.-P.; Hopkins, P. E. Charge-Induced Disorder Controls the Thermal Conductivity of Entropy-Stabilized Oxides. *Adv. Mater.* **2018**, *30* (51), 1805004.
(90) Yang, K.; Bryce, K.; Yao, T.; Zhao, D.; Lian, J. Chemical durability and corrosion-induced microstructure evolution of compositionally complex titanate pyrochlore waste forms with uranium incorporation. *J. Eur. Ceram. Soc.* **2024**, *44*, 1102−1114.
(91) Bryce, K.; Yang, K.; Yao, T.; Lian, J. Chemical durability of multicomponent lanthanide zirconate solid solutions. *Ceram. Int.* **2023**, *49*, 39196−39204.
(92) Majee, B. P.; Bryce, K.; Huang, L.; Lian, J. High temperature steam corrosion of $LuPO_4$ and high-entropy rare earth phosphates in the presence of $Al(OH)_3$ and $Si(OH)_4$ impurities. *npj Mater. Degrad.* **2025**, *9*, 76.
(93) Wang, H.; Hu, H.; Wang, Z.; zhou, L.; Liu, C.; Song, Y.; Zhang, C.; Li, Y. A reevaluation of radiation resistance in high-entropy pyrochlores: The role of entropy. *J. Eur. Ceram. Soc.* **2025**, *45*, 117462.
(94) Yoo, C.-Y.; Kim, S.-J. Dimensional modification of oxyfluoride lattice: Preparation and structure of $A'ANb_2O_6F$ (A′=Na, K, A = Ca, Sr). *J. Phys. Chem. Solids* **2008**, *69*, 1475−1478.
(95) Gerasimova, Y. V.; Oreshonkov, A. S.; Ivanenko, A. A.; Molokeev, M. S.; Isaenko, L. I.; Flerov, I. N.; Bogdanov, E. V.; Gorev, M. V.; Kartashev, A. V.; Krylov, A. S. Structural, spectroscopic, and thermophysical investigations of the oxyfluorides $CsZnMoO_3F_3$ and $CsMnMoO_3F_3$ with the pyrochlore structure. *Phys. Solid State* **2014**, *56*, 599−605.
(96) Zhao, Y.; Ai, Q.; Sun, S.-K.; Tan, S.-H.; Liang, X.; Guo, W.-M.; Lin, H. t. Densification of Ba_2NaIO_6 ceramic wasteform for enhanced iodine immobilization. *J. Nucl. Mater.* **2025**, *616*, 156062.
(97) Han, G.; Li, T.; Xu, X.; Lee, J.; Qiu, G.; Sequeira, S. G.; Ajith, A.; Oses, C. The search for high-entropy fuel-cell catalysts using disorder descriptors. *Nano Futur* **2025**, *9*, 045001.
(98) Reid, A. F.; Li, C.; Ringwood, A. E. High-pressure silicate pyrochlores, $Sc_2Si_2O_7$ and $In_2Si_2O_7$. *J. Solid State Chem.* **1977**, *20*, 219−226.
(99) Chen, D.; Xu, R. Hydrothermal synthesis and characterization of $La_2M_2O_7$ (M = Ti, Zr) powders. *Mater. Res. Bull.* **1998**, *33*, 409−417.
(100) Arpino, K. E.; Trump, B. A.; Scheie, A. O.; McQueen, T. M.; Koohpayeh, S. M. Impact of stoichiometry of $Yb_2Ti_2O_7$ on its physical properties. *Phys. Rev. B* **2017**, *95*, 094407.
(101) Hector, A. L.; Wiggin, S. B. Synthesis and structural study of stoichiometric $Bi_2Ti_2O_7$ pyrochlore. *J. Solid State Chem.* **2004**, *177*, 139−145.
(102) Haghighirad, A. A.; Ritter, F.; Assmus, W. Crystal growth of $A_2V_2O_7$ (A = Y, Er, and Dy) pyrochlores using high pressure. *Cryst. Growth Des.* **2008**, *8*, 1961−1965.
(103) Murugesan, M.; Nagavenkatesh, K. R.; Devendran, P.; Nallamuthu, N.; Uthayakumar, T. Facile synthesis of $Zn_2V_2O_7$/RGO nanocomposite for enhancing the electrochemical performance and evaluating the supercapacitor device. *Inorg. Chem. Commun.* **2024**, *165*, 112544.
(104) Shimakawa, Y.; Kubo, Y.; Hamada, N.; Jorgensen, J. D.; Hu, Z.; Short, S.; Nohara, M.; Takagi, H. Crystal structure, magnetic and transport properties, and electronic band structure of $A_2Mn_2O_7$ pyrochlores (A = Y, In, Lu, and Tl). *Phys. Rev. B* **1999**, *59*, 1249−1257.
(105) Subramanian, M. A.; Toby, B. H.; Ramirez, A. P.; Marshall, W. J.; Sleight, A. W.; Kwei, G. H. Colossal magnetoresistance without Mn^{3+}/Mn^{4+} double exchange in the stoichiometric pyrochlore $Tl_2Mn_2O_7$. *Science* **1996**, *273*, 81−84.
(106) Greedan, J. E.; Raju, N. P.; Subramanian, M. A. Structure and magnetic properties of the pyrochlore $Sc_2Mn_2O_7$. *Solid State Commun.* **1996**, *99*, 399−402.
(107) Li, H.; Li, Y.; Li, N.; Zhao, Y.; Zhu, H.; Zhu, P.; Wang, X. A comparative study of high pressure behaviors of pyrochlore-type and thortveitite-type $In_2Ge_2O_7$. *RSC Adv.* **2015**, *5*, 44121−44127.
(108) Ashan, M.; Mersal, G. A. M.; Fallatah, A. M.; Ibrahim, M. M.; Ahmad, K.; El-Bahy, Z. M. Achieving superior supercapacitive

https://doi.org/10.1021/prechem.5c00467
Precis. Chem. XXXX, XXX, XXX−XXX

performance with rGO-integrated pyrochlore type $Ce_2Zr_2O_7$. *Mater. Sci. Semicond. Proc.* **2025**, *185*, 108912.
(109) Wang, L.; Li, J.; Xie, H.; Chen, Q.; Xie, Y. Solubility, structure transition and chemical durability of Th-doped $Nd_2Zr_2O_7$ pyrochlore. *Prog. Nucl. Energy* **2021**, *137*, 103774.
(110) Koohpayeh, S. M.; Wen, J.-J.; Trump, B. A.; Broholm, C. L.; McQueen, T. M. Synthesis, floating zone crystal growth and characterization of the quantum spin ice $Pr_2Zr_2O_7$ pyrochlore. *J. Cryst. Growth* **2014**, *402*, 291−298.
(111) Samizo, A.; Minohara, M.; Kikuchi, N.; Ando, K.; Mazuka, Y.; Nishio, K. Disorders and oxygen vacancies in p-type $Sn_2B_2O_7$ (B = Nb, Ta): Role of the B-site element. *J. Am. Ceram. Soc.* **2023**, *106*, 1540−1546.
(112) Łukaszewicz, K.; Pietraszko, A.; Stepień-Damm, J.; Kolpakova, N. N. Temperature dependence of the crystal structure and dynamic disorder of cadmium in cadmium pyroniobates [$Cd_2Nb_2O_7$ and $Cd_2Ta_2O_7$]. *Mater. Res. Bull.* **1994**, *29*, 987−992.
(113) Moritomo, Y.; Xu, S.; Machida, A.; Katsufuji, T.; Nishibori, E.; Takata, M.; Sakata, M.; Cheong, S.-W. Chemical pressure control of exchange interaction in Mo pyrochlore. *Phys. Rev. B* **2001**, *63*, 144425.
(114) Muller, O.; White, W. B.; Roy, R. Crystal chemistry of some technetium-containing oxides. *J. Inorg. Nucl. Chem.* **1964**, *26*, 2075−2086.
(115) Rodriguez, E. E.; Poineau, F.; Llobet, A.; Thompson, J. D.; Seshadri, R.; Cheetham, A. K. Preparation, magnetism and electronic structures of cadmium technetates. *J. Mater. Chem.* **2011**, *21*, 1496−1502.
(116) Gai, X.; Qu, J.; Zhang, N.; You, C.; Zhang, F.; Lv, T.; Tao, Q.; Zhu, P.; Li, Y.; Wang, X. Pressure-Induced Suppression of Static Disorder and Lattice Distortion in Pyrochlore $Bi_2Ru_2O_7$. *J. Phys. Chem. C* **2024**, *128*, 7306−7315.
(117) Munenaka, T.; Sato, H. A novel pyrochlore ruthenate: $Ca_2Ru_2O_7$. *J. Phys. Soc. Jpn.* **2006**, *75*, 103801.
(118) Klein, W.; Kremer, R. K.; Jansen, M. Hg_2 Ru_2O_7, a new pyrochlore showing a metal−insulator transition. *J. Mater. Chem.* **2007**, *17*, 1356−1360.
(119) Miao, X.; Zhang, J.; Hu, Z.; Zhou, S. Modulating Electronic Correlations in Ruthenium Oxides for Highly Efficient Oxygen Evolution Reaction. *Precis. Chem.* **2025**, *3*, 72−81.
(120) Matsumoto, A.; Cai, Z.-X.; Fujita, T. Synthesis of pyrochlore oxides containing Ir and Ru for efficient oxygen evolution reaction. *Materials* **2022**, *15*, 6107.
(121) Kraidy, A. F.; Yapi, A. S.; El Marssi, M.; Penton Madrigal, A.; Gagou, Y. Structural Refinement and Optoelectrical Properties of $Nd_2Ru_2O_7$ and $Gd_2Ru_2O_7$ Pyrochlore Oxides for Photovoltaic Applications. *Materials* **2024**, *17*, 2571.
(122) Longo, J. M.; Raccah, P. M.; Kafalas, J. A.; Pierce, J. W. Preparation and structure of a pyrochlore and perovskite in the $BiRhO_{3+x}$ system. *Mater. Res. Bull.* **1972**, *7*, 137−146.
(123) Zhang, S.; Xu, J.; Lu, C.; Ouyang, R.; Ma, J.; Zhong, X.; Fang, X.; Xu, X.; Wang, X. Preparation method investigation and structure identification by XRD and Raman techniques for $A_2B_2O_7$ composite oxides. *J. Am. Ceram. Soc.* **2024**, *107*, 3475−3496.
(124) Zhang, J.; Wang, D.; Lai, L.; Fang, X.; Xu, J.; Xu, X.; Zhang, X.; Liu, J.; Peng, H.; Wang, X. Probing the reactivity and structure relationship of $Ln_2Sn_2O_7$ (Ln = La, Pr, Sm and Y) pyrochlore catalysts for CO oxidation. *Catal. Today* **2019**, *327*, 168−176.
(125) Mizoguchi, H.; Eng, H. W.; Woodward, P. M. Probing the electronic structures of ternary perovskite and pyrochlore oxides containing Sn^{4+} or Sb^{5+}. *Inorg. Chem.* **2004**, *43*, 1667−1680.
(126) Zhou, H. D.; Wiebe, C. R.; Janik, J. A.; Vogt, B.; Harter, A.; Dalal, N. S.; Gardner, J. S. Spin glass transitions in the absence of chemical disorder for the pyrochlores $A_2Sb_2O_7$ (*A* = Mn, Co, Ni). *J. Solid State Chem.* **2010**, *183*, 890−894.
(127) Sidey, V. I.; Milyan, P. M.; Semrad, O. O.; Solomon, A. M. X-ray powder diffraction studies and bond-valence analysis of $Hg_2Sb_2O_7$. *J. Alloys Compd.* **2008**, *457*, 480−484.
(128) Weber, F. A.; Schleid, T. Pr_2 Te_2O_7: A Praseodymium (III) Oxide Oxotellurate (IV) According to $Pr_2O(TeO_3)_2$ with Pyrochlore-Type Crystal Structure. *Z. Anorg. Allg. Chem.* **2000**, *626*, 1285−1287.
(129) Shlyakhtina, A. V.; Knotko, A. V.; Boguslavskii, M. V.; Stefanovich, S. Y.; Kolbanev, I. V.; Larina, L. L.; Shcherbakova, L. G. Effect of non-stoichiometry and synthesis temperature on the structure and conductivity of $Ln_{2+x}M_{2-x}O_{7-x/2}$ (Ln = Sm−Gd; M= Zr, Hf; *x*= 0−0.286). *Solid State Ion* **2007**, *178*, 59−66.
(130) Redkin, A. F.; Ionov, A. M.; Kotova, N. P. Hydrothermal synthesis of pyrochlores and their characterization. *Phys. Chem. Miner.* **2013**, *40*, 733−745.
(131) Sakai, H.; Yoshimura, K.; Ohno, H.; Kato, H.; Kambe, S.; Walstedt, R. E.; Matsuda, T. D.; Haga, Y.; Onuki, Y. Superconductivity in a pyrochlore oxide, $Cd_2Re_2O_7$. *J. Phys.: Condens. Matter* **2001**, *13*, L785.
(132) Donohue, P. C.; Longo, J. M.; Rosenstein, R. D.; Katz, L. The preparation and structure of cadmium rhenium oxide, $Cd_2Re_2O_7$. *Inorg. Chem.* **1965**, *4*, 1152−1153.
(133) Abakumov, A. M.; Shpanchenko, R. V.; Antipov, E. V.; Kopnin, E. M.; Capponi, J. J.; Marezio, M.; Lebedev, O. I.; Van Tendeloo, G.; Amelinckx, S. Synthesis and Structural Study of $Pb_2Re_2O_{7-x}$Pyrochlores. *J. Solid State Chem.* **1998**, *138*, 220−225.
(134) Reading, J.; Gordeev, S.; Weller, M. T. The synthesis, structure and properties of $Hg_2Os_2O_7$. *J. Mater. Chem.* **2002**, *12*, 646−650.
(135) Yamaura, J.-I.; Yonezawa, S.; Muraoka, Y.; Hiroi, Z. Crystal structure of the pyrochlore oxide superconductor KOs_2O_6. *J. Solid State Chem.* **2006**, *179*, 336−340.
(136) Converse, E. S.; Li, J.; Haskel, D.; LaBarre, P. G.; Ramirez, A. P.; Subramanian, M. A. Os^{4+} Instability in the Pyrochlore Structure: $Tl_{2-x}Bi_xOs_2O_{7-y}$. *Inorg. Chem.* **2020**, *59*, 1227−1233.
(137) Vlášková, K.; Colman, R. H.; Klicpera, M. Synthesis of $Er_2Ir_2O_7$ pyrochlore iridate by solid-state-reaction and CsCl flux method. *Mater. Chem. Phys.* **2021**, *258*, 123868.
(138) Shapiro, M. C.; Riggs, S. C.; Stone, M. B.; de la Cruz, C. R.; Chi, S.; Podlesnyak, A. A.; Fisher, I. R. Structure and magnetic properties of the pyrochlore iridate $Y_2Ir_2O_7$. *Phys. Rev. B* **2012**, *85*, 214434.
(139) Chien, C. L.; Sleight, A. W. Mössbauer effect studies of europium pyrochlores. *Phys. Rev. B* **1978**, *18*, 2031.
(140) Mao, Y.; Li, G.; Sun, Y.; Feng, S. Hydrothermal synthesis and characterization of $Bi_2Pb_2O_7$ with pyrochlore structure. *J. Solid State Chem.* **2000**, *149*, 314−319.
(141) Hacking, M. T., Mendeleev: A Python resource for properties of chemical elements, https://mendeleev.readthedocs.io/en/stable/ (2024). Accessed June 24, 2025.
(142) Wu, K.; Wang, F.; Liao, Q.; Zhu, H.; Liu, D.; Zhu, Y. Synthesis of pyrochlore-borosilicate glass-ceramics for immobilization of high-level nuclear waste. *Ceram. Int.* **2020**, *46*, 6085−6094.
(143) Jiang, M.; Mir, A. H.; Bahri, M.; Zhang, Y.; Arnold, K.; Browning, N.; Whittle, K.; Patel, M. Combined effects of radiation damage and He accumulation in $Y_2Ti_2O_7$ borosilicate glass-ceramic composites. *J. Nucl. Mater.* **2025**, *617*, 156103.
(144) Chen, H.; Marcial, J.; Ahmadzadeh, M.; Patil, D.; McCloy, J. Partitioning of rare earths in multiphase nuclear waste glass-ceramics. *Int. J. Appl. Glass Sci.* **2020**, *11*, 660−675.
(145) Gregg, D. J.; McCloy, J. S.; Vienna, J. D.; Macfarlane, A. M.; Weber, W. J.; Lumpkin, G. R. Glass and ceramic nuclear waste forms: The scientific battle. *Bull. At. Sci.* **2025**, *81*, 3−16.
(146) Divilov, S.; Eckert, H.; Hicks, D.; Oses, C.; Toher, C.; Friedrich, R.; Esters, M.; Mehl, M. J.; Zettel, A. C.; Lederer, Y.; Zurek, E.; Maria, J.-P.; Brenner, D. W.; Campilongo, X.; Filipović, S.; Fahrenholtz, W. G.; Ryan, C. J.; DeSalle, C. M.; Crealese, R. J.; Wolfe, D. E.; Calzolari, A.; Curtarolo, S. Disordered enthalpy-entropy descriptor for high-entropy ceramics discovery. *Nature* **2024**, *625* (7993), 66−73.
(147) Kaufmann, K.; Maryanovsky, D.; Mellor, W. M.; Zhu, C.; Rosengarten, A. S.; Harrington, T. J.; Oses, C.; Toher, C.; Curtarolo,

https://doi.org/10.1021/prechem.5c00467
Precis. Chem. XXXX, XXX, XXX−XXX

S.; Vecchio, K. S. Discovery of high-entropy ceramics via machine learning. *npj Comput. Mater.* **2020**, *6*, 42.
(148) Sanders, M. B.; Krizan, J. W.; Plumb, K. W.; McQueen, T. M.; Cava, R. J. $NaSrMn_2F_7$, $NaCaFe_2F_7$, and $NaSrFe_2F_7$: novel single crystal pyrochlore antiferromagnets. *J. Phys.: Condens. Matter* **2017**, *29*, 045801.
(149) Oliveira, E. A.; Guedes, I.; Ayala, A. P.; Gesland, J.-Y.; Ellena, J.; Moreira, R. L.; Grimsditch, M. Crystal structure and vibrational spectrum of the $NaCaMg_2F_7$ pyrochlore. *J. Solid State Chem.* **2004**, *177*, 2943−2950.
(150) van Uitert, L. G. Relations Between Normal Boiling Point and Melting Point for Simple Halides and Oxides. *J. Am. Ceram. Soc.* **1983**, *66*, 380−382.
(151) Ma, Z.; Wang, Y.; Rui, T.; Lan, Y.; Lu, L.; Yu, Y.; Deng, M.; Lan, T.; Zhao, Z.; Teng, Z.; Zhang, H. Synthesis, microstructures, and aqueous chemical durability of high-entropy pyrochlore ceramic $Eu_2B_2O_7$ (B = Ti, Zr, Sn, Hf, Nb, and Ce) for nuclear waste immobilization. *J. Eur. Ceram. Soc.* **2026**, *46*, 117844.
(152) Toby, B. H.; Von Dreele, R. B. GSAS-II: the genesis of a modern open-source all purpose crystallography software package. *J. Appl. Crystallogr.* **2013**, *46* (2), 544−549.
(153) Thermo Fisher Scientific, XPS Depth Profiling, https://www.thermofisher.com/us/en/home/materials-science/learning-center/surface-analysis/monatomic-depth-profiling.html (2025). Accessed Dec 30, 2025.
(154) Moore, C.; Moon, J.; Chidambaram, D. Using sputtering parameters to mitigate argon ion sputtering induced reduction of nickel in XPS. *Appl. Surf. Sci.* **2024**, *659*, 159876.
(155) Isaacs, M. A.; Davies-Jones, J.; Davies, P. R.; Guan, S.; Lee, R.; Morgan, D. J.; Palgrave, R. Advanced XPS characterization: XPS-based multi-technique analyses for comprehensive understanding of functional materials. *Mater. Chem. Front.* **2021**, *5*, 7931−7963.
(156) ASTM International, *Standard Test Methods for Determining Chemical Durability of Nuclear, Hazardous, and Mixed Waste Glasses: The Product Consistency Test (PCT)*, Tech. Rep., ASTM International (2021).
(157) Chee, T.-S.; Lee, S.; Ng, W. J.; Akmal, M.; Ryu, H. J. Bi^0−Reduced Graphene Oxide Composites for the Enhanced Capture and Cold Immobilization of Off-Gas Radioactive Iodine. *ACS Appl. Mater. Interfaces* **2023**, *15*, 40438−40450.

https://doi.org/10.1021/prechem.5c00467
Precis. Chem. XXXX, XXX, XXX−XXX